Universidade do Estado do Rio de Janeiro

Centro de Tecnologia e Ciências

Faculdade de Engenharia

Gustavo Charles Peixoto de Oliveira
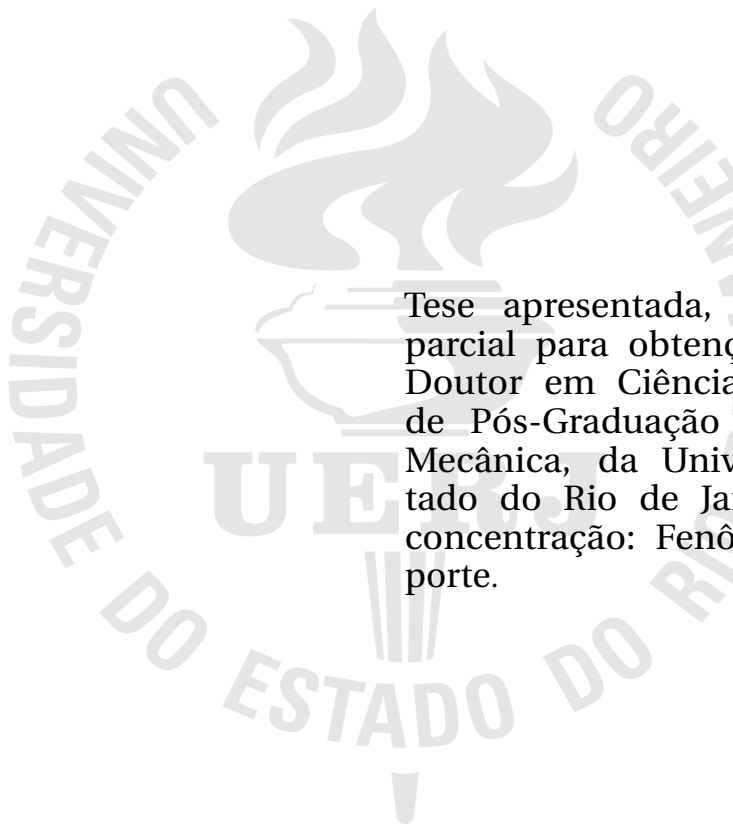
Drop Jet in Crossflow: ALE/Finite Element Simulations and Interfacial Effects

Rio de Janeiro

2015

Gustavo Charles Peixoto de Oliveira

Drop Jet in Crossflow: ALE/FEM Simulations and Interfacial Effects

Tese apresentada, como requisito parcial para obtenção do título de Doutor em Ciências, ao Programa de Pós-Graduação em Engenharia Mecânica, da Universidade do Estado do Rio de Janeiro. Área de concentração: Fenômenos de Transporte.

Advisor: Prof. Ph.D. Norberto Mangiavacchi

Rio de Janeiro

2015

Autorizo, apenas para fins acadêmicos e científicos, a reprodução total ou parcial desta dissertação, desde que citada a fonte.

_____   _____

              Assinatura   Data

Gustavo Charles Peixoto de Oliveira

Drop Jet in Crossflow: ALE/Finite Element Simulations and Interfacial Effects

Tese apresentada, como requisito parcial para obtenção do título de Doutor em Ciências, ao Programa de Pós-Graduação em Engenharia Mecânica, da Universidade do Estado do Rio de Janeiro. Área de concentração: Fenômenos de Transporte.

Aprovado em: 20 de fevereiro de 2015

Banca Examinadora:

Prof. Ph.D. Norberto Mangiavacchi (Orientador)
Faculdade de Engenharia - UERJ

Prof. Ph.D. Carlos Antonio de Moura
Instituto de Matemática e Estatística - UERJ

Prof. Ph.D. Leonardo Santos de Brito Alves (Co-orientador)
Universidade Federal Fluminense

Prof. D.Sc. Álvaro Luiz Gayoso de Azeredo Coutinho
Universidade Federal do Rio de Janeiro

Prof. D.Sc. José Henrique Carneiro de Araújo
Universidade Federal Fluminense

Rio de Janeiro

2015

DEDICATION

I dedicate this thesis to God, my *Abba* and manly father, who has bestowed upon me this laurel, even after the most thoughtful mind inquires why; to the sovereignty of the Brazilian science, even though my labour only sows a mere mustard seed.

ACKNOWLEDGMENTS

Let my teaching drop as the rain, my speech distill as the dew, as the droplets on the fresh grass and as the showers on the herb. (The Song of Moses)

Deuteronomy 32:2

RESUMO

OLIVEIRA, Gustavo Charles P. de *Drop Jet in Crossflow: ALE/Finite Element Simulations and Interfacial Effects.* 218 f. Tese (Doutorado em Engenharia Mecânica) - Faculdade de Engenharia, Universidade do Estado do Rio de Janeiro (UERJ), Rio de Janeiro, 2015.

Um código computacional para escoamentos bifásicos incorporando metodologia híbrida entre o Método dos Elementos Finitos e a descrição Lagrangeana-Euleriana Arbitrária do movimento é usado para simular a dinâmica de um jato transversal de gotas na zona primária de quebra. Os corpos dispersos são descritos por meio de um método do tipo *front-tracking* que produz interfaces de espessura zero através de malhas formadas pela união de elementos adjacentes em ambas as fases e de técnicas de refinamento adaptativo. Condições de contorno periódicas são implementadas de modo variacionalmente consistente para todos os campos envolvidos nas simulações apresentadas e uma versão modificada do campo de pressão é adicionada à formulação do tipo "um-fluido" usada na equação da quantidade de movimento linear. Simulações numéricas diretas em três dimensões são executadas para diferentes configurações de líquidos imiscí veis compatíveis com resultados experimentais encontrados na literatura. Análises da hidrodinâmica do jato transversal de gotas nessas configurações considerando trajetórias, variação de formato de gota, espectro de pequenas perturbações, além de aspectos complementares relativos à qualidade de malha são apresentados e discutidos.

Palavras-chave: Jato Transversal; Lagrangeano-Euleriano Arbitrário; Elementos Finitos; Escoamento Bifásico; Condições de Contorno Periódicas.

ABSTRACT

A two-phase flow computational code taking a hybrid Arbitrary Lagrangian-Eulerian description of movement along with the Finite Element Method is used to simulate the dynamics of an incompressible drop jet in crossflow in the primary breakup zone. Dispersed entities are described by means of a front-tracking method which produces zero-thickness interfaces through contiguous element meshing and adaptive refinement techniques. Periodic boundary conditions are implemented in a variationally consistent way for all the scalar fields involved in the presented simulations and a modified version of the pressure field is added to the "one-fluid" formulation employed in the momentum equation. Three-dimensional direct numerical simulations for different flow configurations of immiscible liquids pertinent to experimental results found in literature. Analyses of the hydrodynamics of the drop jet in crossflow in these configurations considering trajectories, drop shape variations, spectrum of small disturbances, besides additional aspects relating to mesh quality are presented and discussed.

Keywords: Jet in Crossflow; Arbitrary Lagrangian-Eulerian; Finite Element; Two-Phase Flow; Periodic Boundary Conditions.

LIST OF FIGURES

LIST OF TABLES

LIST OF SYMBOLS

Acronyms

ALE   Arbitrary Lagrangian-Eulerian

CAD   Computer-Aided Design

CFD   Computational Fluid Dynamics

CIP   Cubic Interpolated Profile

CK   Chemical Kinetics

CSF   Continuum Surface Force

CVP   Counter-Rotating Vortex Pair

DBC   Dirichlet Boundary Conditions

DJICF Drop Jet in Crossflow

DOFs Degrees of Freedom

FE   Finite Element

FEM   Finite Element Method

FFR   Fixed Frame Reference

FFT   Fourier Fast Transform

JICF   Jet in Crossflow

KH   Kelvin-Helmholtz

LBB   Ladyzhenskaya-Babuska-Brezzi

LSA   Linear Stability Analysis

LS   Level-Set

MAC   Marker-and-Cell

MFR   Moving Frame Reference

NBC   Neumann Boundary Conditions

OBC   Open Boundary Conditions

PBC   Periodic Boundary Conditions

RT   Rayleigh-Taylor

VOF   Volume of Fluid

Greek letters

β_1 mesh parameter: pure Lagrangian motion

β_2 mesh parameter: neighbourhood-based velocity smoothing

β_3 mesh parameter: elastic-based velocity Laplacian smoothing

α backward displacement vector

χ position in the reference domain

δ δ function

δ_ζ distribution over an interface

η distance to interface, or interface node

Γ boundary

γ_1 mesh parameter: tangent iterface velocity magnitude

γ_2 mesh parameter: elastic-based velocity node relocation

ι cardinality of nodes

ι_p cardinality of pressure/scalar points

ι_v cardinality of velocity points

κ curvature

λ barycentric coordinate, or jet-to-crossflow velocity ratio

μ	dynamic viscosity
ν	kinematic viscosity
Ω	domain
ω	frequency
$\overline{\Omega}$	closure of Ω
ϕ	arbitrary scalar quantity
ϕ	mapping function from referential domain to the spatial domain
Ψ	mass concentration
ψ	flatness ratio
$\boldsymbol{\Psi}$	mapping function from referential domain to the material domain
ρ	density
σ	surface tension
$\boldsymbol{\Sigma}$	surface tension matrix
τ	time
λ	second viscosity
μ	viscosity ratio $\frac{\mu_1}{\mu_2}$
ϕ	elongation ratio
ρ	density ratio $\frac{\rho_1}{\rho_2}$
φ	shape function
φ	mapping function from material domain to spatial domain
ϖ	circulation
ϱ	mass diffusivity coefficient
ξ	Lagrangian interface point

ζ continuous surface

Roman letters

A area

a wave amplitude, or peak

B body

$\mathbf{bc}$ boundary condition discrete vector

F abstract source vector of fluid variables

$\boldsymbol{\Phi}$ abstract unknown vector of fluid variables

X particle pathline

$\mathbf{b}$ body force, or discrete vector, or binormal vector

$\check{\mathbf{v}}$ particle velocity in the referential domain

$\mathbf{c}$ relative velocity between the fluid and the mesh

d differential

$\mathbf{D}$ discrete divergent matrix

e arbitrary function

e element index

$\mathbf{E}$ discrete pressure-related matrix

$\mathbf{e}$ error

F face of element

f frequency

$\mathbf{F}$ tensor, or force

$\mathbf{f}$ interfacial force

g gravity

$\mathbf{G}$	discrete gradient matrix
$\mathbf{g}$	gravity field
H	Heaviside function
$\mathbf{h}$	Heaviside function discrete vector
$\mathbf{I}$	identity tensor or matrix
$\mathbf{j}$	flux of mass concentration
k	wave number
$\mathbf{K}$	discrete viscosity-related matrix
l	line element, or edge length
L	length
m	dimension
$\mathbf{M}$	mass matrix
$\mathbf{n}$	normal unit vector
$\mathbf{o}$	origin of fixed reference frame
p	hydrostatic pressure
$\tilde{\mathbf{p}}$	discrete periodic pressure vector
$\mathbf{p}$	"pull" vector, or discrete pressure vector
$\mathbf{r}$	r.h.s. discrete vector
s	curve element
$\mathbf{s}$	surface force
T	simplex, or triangle, or tetrahedron
t	time instant
$\tilde{p}$	periodic pressure

T   tensor

t   tangent unit vector

u arbitrary function

U velocity

v   fluid velocity

$\mathbf{v}_e$ "elastic" velocity

$\hat{\mathbf{v}}$ mesh velocity

w arbitrary weight function

w   weight function discrete vector, or arbitrary vector

X   position in the material domain

x   position in the spatial domain

Superscripts

$(\cdot)^1$ dispersed phase

$(\cdot)^2$ continuous phase

$(\cdot)^{\#}$ intermediary, or provisional

$(\cdot)^i$ indexing

$(\cdot)^m$ dimension

$(\cdot)^n$ iterative time step

$(\cdot)^p$ interpolation order

$(\cdot)^r$ integration order

$(\cdot)^{\sigma}$ relative to surface tension

$(\cdot)^*$ dimensionless

$(\cdot)^T$ transpose

Subscripts

$(\cdot)_0$ initial condition, or compact support

$(\cdot)_1$ arbitrary index, or relative to dispersed phase

$(\cdot)_2$ arbitrary index, or relative to continuous phase

$(\cdot)_A$ relative to area

$(\cdot)_a$ arrival

$(\cdot)_\beta$ relative to pressure gradient

$(\cdot)_c$ relative to center of mass, or centroid

$(\cdot)_{corr}$ correction

$(\cdot)_{crit}$ critical

$(\cdot)_D$ Dirichlet

$(\cdot)_d$ departure

$(\cdot)_e$ element, or elementary

$(\cdot)_f$ final

$(\cdot)_h$ relative to refinement

$(\cdot)_\#$ provisional

$(\cdot)_I$ relative to interface

$(\cdot)_{i,j}$ node or point indexing

$(\cdot)_L$ relative to lumped

$(\cdot)_\lambda$ relative to jet-to-crossflow velocity ratio

$(\cdot)_m$ mean, or intermediary

$(\cdot)_{mov}$ moving

$(\cdot)_N$ Neumman

$(\cdot)_{NS}$ relative to Navier-Stokes

$(\cdot)_P$ periodic

$(\cdot)_\partial$ relative to boundary

$(\cdot)_\phi$ relative to elongation

$(\cdot)_\Psi$ relative to mass concentration

$(\cdot)_\psi$ relative to flatness

$(\cdot)_{ref}$ reference

$(\cdot)_{rel}$ relative

$(\cdot)_\rho$ relative to phase

$(\cdot)_t$ relative to time, or compact support

Symbols

$A_{\mathscr{I}}^{max}$ number of tetrahedra of maximum quality

$*$ interelement Neumman contributions

$\square$ interelement Neumman contributions

$\bullet$ interelement Neumman contributions

Ca Capillary number

$\mathscr{A}$ periodic copying matrix-model

$\mathscr{B}$ "bubble" function space

$\mathscr{E}$ error in modulus

$\mathscr{H}$ Sobolev space

$\mathscr{L}$ Lebesgue space

$\mathscr{M}$ MINI element's function space

$\mathscr{N}$ set of the vectors normal to a body's surface

$\mathcal{O}$ order

$\mathcal{P}$ space of polynomial functions

$\mathcal{Q}$ space of trial functions for pressure

$\mathcal{R}$ space of weight functions

$\mathcal{S}$ space of trial functions for velocity

$\mathcal{U}$ periodic copying vector-model

$\mathcal{V}$ space of weight functions

$\mathcal{X}$ set of the points on a body's surface

$\mathcal{Y}$ set of nodal variables (*ipsis litteris*: degrees of freedom)

$\cdot$ inner product

CFL Courant-Friedrichs-Lewy number

$:$ tensor inner product

dA infinitesimal area

$\delta_{\cdot,\cdot}$ Kronecker's delta

Δt discrete time step

δt infinitesimal time

$\Delta \tau$ continuous time interval

$\Delta \mathbf{x}$ displacement

$\diamond$ interelement Neumman contributions

dim   dimension

$\nabla \cdot$ divergent operator

dl infinitesimal line

$\dfrac{D}{D\tau}$ material derivative operator

$\dfrac{D}{Dt}$ material derivative operator

$\doteq$ "equivalent by input argument to"

dV infinitesimal volume

Eo Eötvös number

Eu Euler number

$\mathbf{e}_i$ canonical unit vectors of $\mathbb{R}^3$

$\mathbf{e}_P$ unit vector of periodic direction

$\Im$ imaginary part of a complex number

$(\cdot,\cdot)$ inner product, or bilinear form, or ordered pair

∇^2 Laplace operator

$\rightsquigarrow$ "is associated to"

$\mathscr{I}_{(T)}$ radius ratio quality measure of T

$\mathscr{T}_h$ tessellation, or triangulation, or tetrahedralization

$\mathring{\Omega}$ interior of Ω

E disturbance maximum energy

L differential operator

P,Q projection operators

R fixed reference frame

$\hat{\mathsf{R}}$ moving reference frame

N Archimedes number

∇ gradient operator

Oh Ohnesorge number

$\oplus$	direct sum
$\otimes$	tensor product
∂	partial derivative, or boundary
Pe	Peclét number
$\mathcal{O}_\%$	mesh quality percentage at a fixed time
R_1, R_2	principal radii of curvatures
$\Re$	real part of a complex number
Re	Reynolds number
$\mathbb{R}^m$	$m-$dimensional real vector space
$\nabla\times$	curl operator
Sc	Schmidt number
St	Strouhal number
$\star$	interelement Neumman contributions
$\mathcal{T}_h^\Gamma$	discrete surface mesh
$\mathcal{T}_h^\Omega$	discrete volume mesh
$\triangle$	interelement Neumman contributions
$\vee$	logical XOR (exclusive "or")
Fr	Froude number
We	Weber number

CONTENTS

INTRODUCTION

Jets in crossflow (JICFs) arise abundantly in diverse technological apparatuses and natural phenomena that range from mixture microdevices, propulsion systems to gaseous plumes in volcanic eruptions. The main feature of JICFs is their empowerment to provide mixture and dilution of substances, which are processed as the jet is issued into an ambient flow either normal or tilted to it.

In engineering and aerodynamics, some applications of JICFs are the following: in airbreathing turbines, the control of gas emissions is achieved by varying the air-fuel mixture ratio through transverse air jet injection in the primary zone of gas turbine combustors; in scramjets, air at supersonic speeds enters in its combustion chamber and the fast reaction process requires rapid transverse fuel penetration, mixing with crossflow, ignition, and sustainment of combustion; thrust vector control, mainly for rocket engines, - inasmuch as the thrust can be altered in direction and, to a limited extent, in magnitude by the deflection of the flow within the rocket engine's nozzle - is caused by the injection of an array of transverse jets; concerning V/STOL aircrafts, such as the Harrier model, an application is concentrated in the "jump" jets, during take-off, hovering, and transition to wing-borne flight in vertical/short take-off and landing.

With respect to environmental purposes, JICFs are observed as smoke plumes exhausting from chimneys in power plants, flare stack gas burners, and effluents pouring into rivers, where the jet is issued in angle to the free stream. JICFs are a model, moreover, for puffs, flames, and turbulent mixing of gases in the atmosphere. Due to the environmental risks, the reduction of pollutant emissions from hydrocarbon-based systems, such as gas turbines and petroleum refineries as well as the lower ejection of nitrogen oxides (NOx), carbon monoxide (CO), and soot into the air evoke immediate decision-making for controlled exhaustions, thereby motivating the research in this area.

On the other hand, the dynamics of nonturbulent immiscible liquid-liquid jets is present in many modern applications, thus opening research branches for the study of drop jets in crossflow (DJICF) developing at microscale. The performance of devices in chemical processes, microfluidics and drug delivery, for instance, is closely based on crossflow shear flows along with dripping and jetting regimes. Crossflow membrane emulsification processes in which the dispersed phase is introduced in the continuous phase by pressure through

a membrane containing one or more pores constitute flows with dense drop interactions. In industry, the capillary breakup of jets of molten oxides at high temperatures, as a final example, is investigated in metal production, steelmaking processes and high-precision solder printing technology.

The comprehension of the physical phenomena associated to DJICFs depend on theoretical, computational, and experimental bases. Under these circumstances, this numerical work is intended to present a study of drop jets in crossflow restricted to the primary breakup zone by using an Arbitrary Lagrangian-Eulerian (ALE)/Finite Element methodology. Dynamic meshes along with the consideration of interfacial effects render key tools to deal with the problems arising from the multifluid/multiphase flow scope such as those contained in this thesis.

1 **LITERATURE REVIEW**

Studies about the JICF have a plentiful history and range each of the experimental, theoretical, and numerical branches broadly. This chapter introduces a conspectus of information devoted to this flow and ends up with the formalization of the purposes of this thesis. We begin with a basic presentation of the general physical aspects of JICF. Sequentially, a review of some selected articles that boosted the scientific progress of this field is given in a medially chronological sense, appending important contributions of the current time to JICF's motifs. Lastly, issues on jet instability and breakup in liquid-liquid systems as well as specific applications of drops in crossflow are presented.

1.1 **Jet in crossflow: physics and models**

As illustrations, Figure 1 displays four great facets of JICF in different situations. First of all, a picture of an aircraft model Harrier - label (a) - shows how the process of vertical short take-off and/or landing (V/STOL) is utterly associated to a crossflow interaction. In second place, an atomized liquid jet in crossflow is viewed as a result of refuelling in an aircraft engine. On the other hand, it is noteworthy to point out how indispensable such regime serves for irrigation, aerosol, and spray technologies. As a third example, now related to the oil industry, the JICF appears as a large plume rising up from a fire at an oil rig in the Gulf of Mexico. Similar behaviour is observed in flare stack gas burners at oil refineries and in big chimneys of chemical industries as displayed in the fourth picture. As can be seen, many situations allow the exploration of the research about JICF configurations.

For the physical evaluation pertinent to the JICF, we refer to the presentation by Rajaratnam [**?**] diagrammed in Figure 2 as a descriptive sectioning of the jet issued normally to the free stream. As explained therein, the stagnation pressure exerted by the free stream is responsible for deflecting the jet. Due to the turbulent mixing developing on the periphery of the jet, the outer layers lose part of their momentum and hence are easily deflected, bringing forth a characteristic kidney shape for the jet. As the jet hits the free stream, there is a central region of relatively shear free flow. This region specified by the length OC is generally known as the potential core region. When the jet-to-crossflow velocity ratio $\lambda^{-1} = \frac{U_j}{U_\infty}$ is relatively greater than 4, the point C is located directly over the center of the jet. For smaller values, the point C is pushed downwind.

Figure 1: Images from internet sites exemplifying physical conditions in which JICF configurations are detected: (a) an AV-8B Harrier aircraft during vertical taking-off process (from [?]); (b) atomization of an aircraft engine liquid fuel jet in a crossflow (from [?]); (c) a large plume rising up from a fire on an oil rig in the Gulf of Mexico (from [?]), and (d) gas flow being expelled out to the atmosphere from the big chimney of the Esjberg Power Station, in Denmark (from [?].
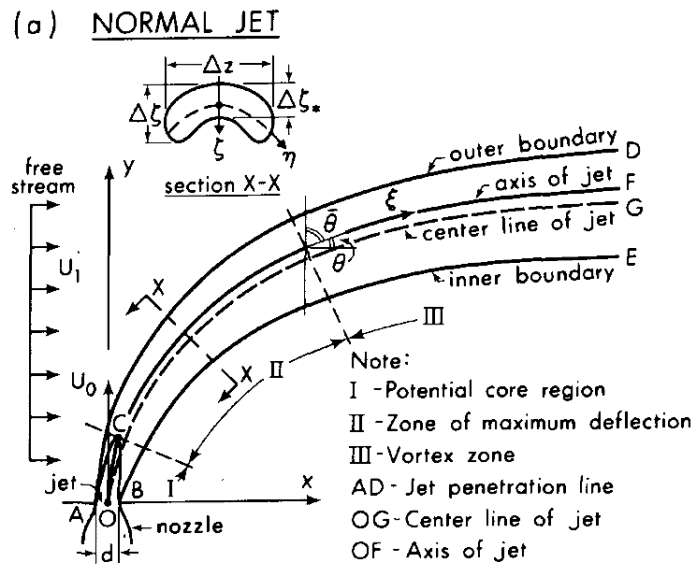
Figure 2: Descriptive sectioning of the jet in crossflow issued normally to the free stream. From [?].

It is known that the length of the potential core varies mainly with the velocity ratio λ^{-1}. Generally, the length of the potential core is less than that of the free jet (i.e. the jet in stagnant surroundings) and approaches asymptotically the free jet value for large values of λ^{-1}. From the end of the potential core, the jet suffers a large deflection in a certain length which is known as the zone of maximum deflection, where mixing cores evolve. The remnant portion of the deflected jet is also referred to as the vortex region, where a pair of counter-rotating vortices (CVP) connected by circulation free fluid shed. Apropos the vortical structures developing in the JICF, three other kinds of patterns are recognized in the literature, beyond the CVP before mentioned, namely, shear-layer vortices, horseshoe vortices, and wake vortices.

Several models were introduced in the literature in attempting to tackle the JICF problem. Among them, fundamental references provided geometrical schemes quite representative, such as that of Coelho and Hunt [?], the almost crowned example of the vortical structures supplied by Fric and Roshko [?], and that one of Lim, New, and Luo [?], all of them reproduced in Figure 3 and Figure 4.
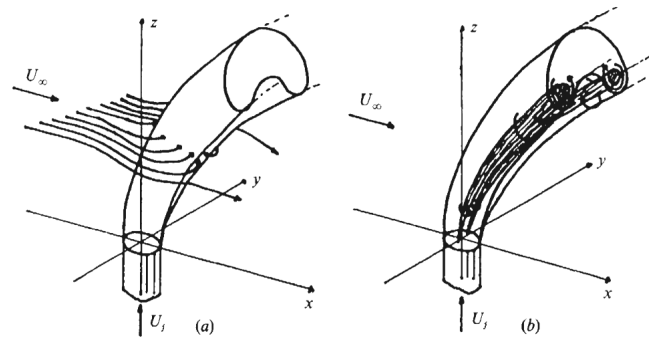
Figure 3: Model of the JICF depicting the entrainment effect caused by the free stream. Extracted from [?].
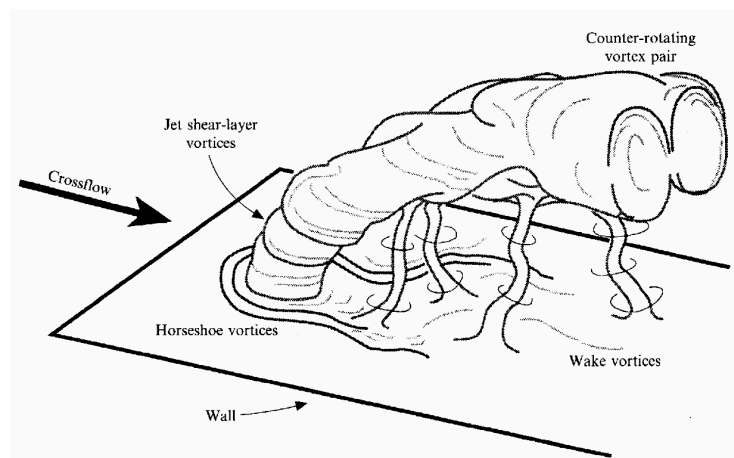
(a)
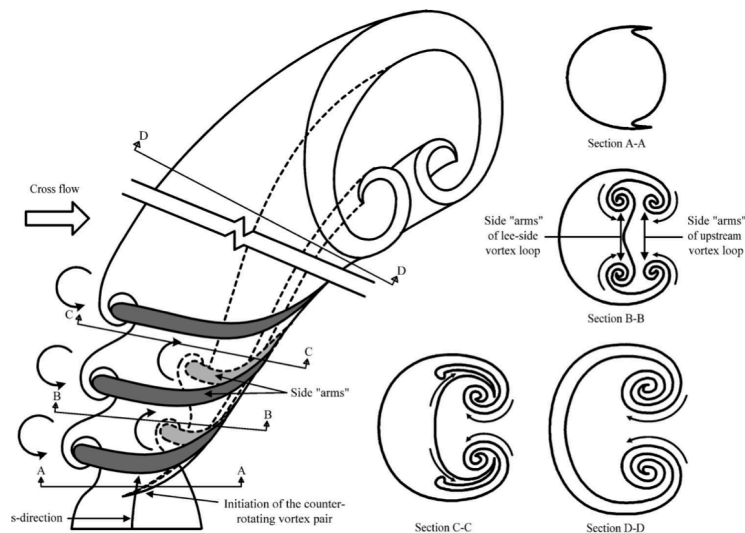
(b)

Figure 4: The jet in crossflow highlighting its rich vortical structures: (a) cartoon extracted from the referential work by Fric and Roshko and (b) drawing taken from Lim, New, and Luo.

1.2 **Jet in crossflow: a summary**

Abramovich [?] was one of the pioneers in describing JICF experiments, focusing on the effect of the jet-to-crossflow velocity ratio λ^{-1} on the jet trajectory. Kamotani and Greber [?], and Kelso, Lim and Perry [?], later, advanced on the study of the CVP.

JICF in parallel to thermal plumes were studied by Moussa and Trischka [?], whereas a denser content related to mixture was developed by Smith and Mungal [?]. In this latter article, a scaling criterion was also proposed by establishing three regions for the flow: a vortex interaction region, the near field region and the far field region.

Coelho and Hunt [?] adduced how the momentum transfer, deflection and entrainment occur in the JICF configuration. They studied inviscid vortex-sheet models and pointed out a shortcoming of a widely inviscid 2D model used to describe transverse jets by asserting that the flow within the pipe was not uniform, but affected by the crossflow.

Around the 1990-2000 decades, papers related to jet excitation, better performance of penetration and mixture in crossflows, beyond jet control techniques were conducted by: Johari, Tougas, and Hermanson [?]; Eroglu and Breidenthal [?]; MCloskey *et al.* [?], and Narayanan, Barooah, and Cohen [?]. Such issues involved wave theory and frequencies, whence initiates the comprehension about the sensitivity of the transverse jet to high frequencies.

Theoretical work and numerical simulations of the JICF are also diversified in the literature. Sykes, Lewellen and Parker [?] were among the pioneers in performing 3D numerical simulations of a turbulent jet issued normal to a uniform free stream. In the sequence, Needham, Riley and Smith [?] built 3D models involving concentrations of vorticity for an inviscid incompressible jet issuing skewed into the ambient flow from a semi-infinite pipe. They began to inquire about the cause of deflection of the jet and argued that the influence of the co-flow distorted it asymmetrically.

Minute examinations of the transverse jet through numerical simulations were carried out by Rudman [?]. His jet configuration was flush-mounted into the wall and a compressible code had to be solved with a high Mach number. Even as Rudman had exposed, Hahn and Choi [?] proceed with the study of the effects of computational time step and grid stretching on the numerical solution of a planar jet injected into a laminar boundary-layer.

In regard to the universe of computational techniques, Yuan, Street, and Ferziger [?] were among those who used LES (Large Eddy Simulations) in transverse jet cases, being the

first researchers to deal with and solve the problem of the turbulent boundary-layer appearing in the jet flush-mounted into a wall. Not long ago, Muppidi and Mahesh [?] used DNS (Direct Numerical Simulations) to study the near field of incompressible round jets in crossflow with the goal of obtaining improved correlations for transverse jet trajectories. Additionally, Keimasi, and Taeibi-Rahni [?] came up with techniques based on RANS (Reynolds-Averaged Navier Stokes) equations for the 3D turbulent flow of square jets injected perpendicularly into a crossflow handling several different turbulence models.

Special contents about JICF are found in Karagozian, Cortelezzi and Soldati [?], in a seemingly ceremonial paper by [?], describing a fifty years history about the transverse jet as well as in meticulous synopses organized by Karagozian [?], [?] and Mahesh [?].

1.3 **Selected research milestone**

JICF research is plenteous; hence, it is infeasible and impractical to build a full and unfailing milestone that wraps each issue in a whole. For this reason, this section will cover a compendium of selected references.

1.3.1 Issues on linear stability

Liquid sheets, stability analysis for inviscid jets and instabilities in viscous jets are issues covered in Lin's book [?], in which we will be anchored to single out important remarks *bis in idem*. Despite its literary worth, other good references about shear flows such as the books by Chandrasekhar [?] and by Schmid and Henningson [?] should be appreciated, though this latter lacks in text about jets. Huerre and Monkewitz [?] is one of the most known papers on local and global instabilities, where spatially developing open shear flows are carefully reviewed.

Batchelor and Gill [?] considered temporally growing disturbances to perform a LSA of the parallel free jet and were followed by Michalke [?], who obtained Strouhal numbers for different momentum thickness of the free jet – the Strouhal number gives a sight of the sensitiveness of open shear flows to perturbations and noises and it is defined by $St = f_{ref}L_{ref}/U_{ref}$. Michalke's results relied on a hyperbolic-tangent velocity profile widely known in literature. In others papers [?], [?], [?] he examined the instability mechanism occurring in mixing layers and concluded that spatially growing disturbances were responsible for it.

When studying mixing singular problems with the free jet under the nonparallel flow hypothesis, Morris [?] included viscous effects in his LSA. For the circular jet, Michalke and Hermann [?] described that the incidence of an increasing external co-flow velocity onto the jet decreased the growth rates of the most unstable disturbance but, at the same time, the Strouhal number increased. For this case, they performed an inviscid LSA and made a simple modification of the free jet hyperbolic-tangent profile. Michalke [?] also obtained theoretical results concerning the instability of axisymmetric jets.

Alves [?] studied the shear-layer instabilities and vorticity evolution associated with the JICF in order to get a better understanding of them. A computational code was developed to perform numerical simulations in association with a LSA. The main purposes of that work relied on applications already described herein as well as on some keypoints. Firstly, the instability mechanism in vogue was that one characterized by velocity-gradient regions where most of the vorticity is concentrated. In fact, the question interlaced was how the KH instability that leads to a vortex roll-up in a free jet was affected by the presence of a crossflow perpendicular to the free jet base state. Secondly, a LSA which resulted from the first goal was the additional benefit to understand phenomena concentrated to the near field. The analysis could be switched accordingly between the inviscid and viscous transverse jet base flows. In third place, the numerical simulations were supported by the existence of linear and nonlinear instabilities developing in the transverse jet.

The JICF base velocity profile is three-dimensional and has a non-negligible azimuthal dependence. In his thesis, Alves employed a perturbation expansion approach, using the crossflow-to-jet velocity ratio λ as the perturbation parameter in order to take into account the nonparallel effects of that flow field. Such an approach decouples the azimuthal modes being investigated and is used in the LSA of both the inviscid and viscous base flow models for the transverse jet. Furthermore, a new approach that considers several azimuthal modes simultaneously was developed and applied to the LSA of the inviscid base flow. Another fact emphasized by Alves was a global stability analysis avoidance. The explication was rooted in the expensive time to obtain time-averaged DNS data to use as a base flow for a stability analysis, since DNS resolves a transient flow field evolution with length scales down to the Kolmogorov's scale. An unresolved problem incurs thereof: the development and selection of an appropriate base flow for the transverse jet with respect to the stability analysis.

After a little time, Alves, Kelly, and Karagozian [?] published a paper with results

supplied by the stability analysis of the inviscid transverse jet, in which both the jet and co-flow had the same density. A correction was made in the solution of Coelho and Hunt [**?**] therein because of an error found in one of the second-order kinematic conditions derived by the authors. Through this correction, the main conclusions of Alves were that positive and negative helical modes for the transverse jet had slightly different growth rates, implying a lack of symmetry for the KH instability arising in the transverse jet. Such an approach was affirmed to be the first mathematical verification that even low-level crossflows can produce weak asymmetries in the transverse jet.

In a two-piece paper series, Megerian *et al.* [**?**] and Alves *et al.* [**?**] showed both experimental and theoretical studies upon the transverse jet. Megerian's study provided a detailed exploration of the near field shear-layer instabilities associated with the transverse jet. Jet injection from nozzles which are flush as well as elevated with respect to the tunnel wall were explored experimentally for jet-to-crossflow velocity ratios λ^{-1} in the range $1 \leq \lambda^{-1} \leq 10$ and with jet Reynolds numbers of 2000 and 3000. The results indicated that the nature of the transverse jet instability is significantly different than that of the free jet, and that the instability changes in character as the crossflow velocity is increased. They proposed explanations for the differences previously observed in transverse jets controlled by strong forcing in order to improve techniques for the transverse jet penetration control, mixing, and spread. On the other hand, Alves presented a local LSA for the subinterval $\lambda^{-1} > 4$ using two different base flows for the transverse jet and predicting the maximum spatial growth rate for the disturbances through a expansion in powers of λ. This way, the free jet results could be reached as $\lambda^{-1} \to \infty$. His results matched accordingly to Megerian's experiments, thus suggesting that the convective instability occurs in ratios above 4 and that the instability is strengthened as λ^{-1} is decreased. Consistency of his findings with experiments provided powerful evidence of the dominance of the convectively unstable axisymmetric mode, at least in the regime $\lambda^{-1} > 4$.

Still considering the expansion in λ, Kelly and Alves [**?**] reached a uniformly valid asymptotic solution for the transverse jet. This exercise was accompanied by a LSA in which the inviscid vortex sheet analysis of Coelho and Hunt was extended so including asymptotic analysis of the viscous shear layers that formed along the boundaries of the jet. The instability that gives rise to the near field vortices after developing an asymptotic solution for the three-dimensional base flow was investigated and its validity for large values of the Reynolds number

and small λ was pointed out. By using asymptotic methods, they derived a solution of the NS equations valid under some conditions for the transverse jet near field. This achievement led to a more accurate description of the basic flow.

Until now the citations were entwined in the sense of a local stability analysis. Some contributions on global stability analysis, in turn, are mentioned forth. Bagheri *et al.* [?], at first glance, went ahead in taking up a simulation-based global stability analysis of the viscous three-dimensional JICF considering a steady exact solution to the NS equations, which showed that the JICF is characterized by self-sustained global oscillations for a jet-to-crossflow velocity ratio of 3. By suppressing global instabilities by selective frequency damping, they asserted that the JICF is, in fact, globally unstable and must be placed into this category of flows. They verified that not only the most unstable global modes with high frequencies are compact and represent localized wave packets on the CVP, but also that the existence of global eigenmodes justifies the global stability approach as an appropriate tool to describe the inherent and dominant dynamics of the JICF.

Davitian *et al.* [?] studied the transition of the transverse jet shear layer to global instability in the near field by quantifying the growth of disturbances at several locations along and about the jet shear layer. Moreover, frequency tracking and response of the transverse jet to very strong single-mode forcing were applied. It was evidenced that the flush transverse jet's near field shear layer becomes globally unstable when λ^{-1} is within or below a critical range near 3. According to the authors, this work is characterized as a support tool to improve strategies for the transverse jet control, since this field has been widely developed.

Ilak *et al.* [?] published a brief comment on the DNS of a jet in crossflow at low values of the jet-to-crossflow velocity ratio λ^{-1}, in which they mention the observation of hairpin-like vortices. A part of this paper is sustained by results from Schlatter's *et al.*work [?]. In the latter, the jet is studied numerically by considering the maximum velocity of the parabolic profile. Their modelling imposed an inhomogeneous boundary condition at the crossflow wall and the results showed that two fundamental frequencies – a high one and another low one – are present in the flow tied to self-sustained oscillations. They used nonlinear DNS, modal decomposition into global linear eigenmodes, and proper orthogonal decompostion modes.

In a recent publication, Ilak *et al.* [?] analyzed a bifurcation found from DNS at low values of the jet-to-crossflow velocity ratio λ^{-1}, precisely occurring at $\lambda^{-1} = 0.675$. As λ^{-1} increased, it was showed that the flow evolved from simple periodic vortex shedding (a

limit cycle) to more complicated quasi-periodic behaviour before coming into turbulence. Additionally, a LSA was also performed to predict qualitative data about the dynamics of the nonlinear effects.

1.3.2 Other references

New, Lim and Luo [?] reported the results of an experimental investigation on the effects of jet velocity profiles on the flow field of a round JICF using laser-induced fluorescence and digital particle-image velocimetry techniques (DPIV). Though top hat and parabolic jet velocity profiles with the mass ratios ranging from 2.3 to 5.8 were considered, in the case of the shear-layer associated to a parabolic profile of JICF, there was an increase in jet penetration and a reduction in the near-field entrainment of crossflow fluid.

DNS was used by Muppidi and Mahesh [?] to study a round turbulent jet in a laminar crossflow. Turbulent kinetic energy budgets were computed for this flow and it was shown that the near field is far from a state of turbulence. Additionally, it was observed in the near field that the peak of kinetic energy production was close to the leading edge, while the peak dissipation was observed toward the trailing edge of the jet. Velocity and turbulent intensity profiles from the simulation were also compared to some profiles obtained from experiments, and a good agreement was exhibited. Emphatic points in that treatise was the observation that past the jet exit, the flow is not close to established canonical flows on which most models appear to be based.

One year later, Muppidi and Mahesh [?] used DNS to study passive scalar transport and mixing in a round turbulent jet, in a laminar crossflow. In this case, the Schmidt number rose up naturally as a nondimensional parameter. The scalar field was used to compute entrainment of the crossflow fluid by the jet. It was shown that the bulk of this entrainment occurs on the downstream side of the jet and the simulations were used to comment on the applicability of the gradient-diffusion hypothesis to compute passive scalar mixing in the flow field.

Denev *et al.* [?] followed a similar path using DNS for the flow with transport of passive scalars and chemical reactions when studying phenomena and chemical reactions in a JICF. Instantaneous mixing of structures and laminar to turbulent flow transition were compared to experimental data with good agreement.

Many others fields of application of JICF have been provided with scientific research

in the recent years, which are out of scope of this thesis. However, some references to further contents are listed here: pulsed jets are discussed by Muldoon *et al.* [?], Sau and Mahesh [?] and Coussement *et al.* [?]; jet penetration and injection into subsonic and supersonic crossflow are studied by Lee *et al.* [?] and Rana, Thornber and Drikakis [?], respectively; applications like oil flare stacks, pollutant dispersion, soot emissions and flame stabilization are cited by Grout *et al.* [?] and Marr *et al.* [?]; finally, acoustic excitation and atomization are topics related by Hsu and Huang [?] and Herrmann [?].

1.4   Instability and breakup in two-fluid jets

This section is devoted to bring forth the overall differences among the physical mechanisms encompassing gas-liquid and liquid-liquid jet configurations by emphasizing the drop formation stage in order to narrow the review to the purposes of this thesis. The physics of jets in its entirety is widely discussed by [?], whose major points relate to small perturbations, breakup, spray formation and non-Newtonian effects.

Several studies about jet instabilities found in literature have their fundamentals upon gas-liquid configurations unlike a minor parcel dedicated to liquid-liquid interfaces. The historical development of the LSA applied to liquid jets issued into another immiscible liquid starts from Tomotika [?], who has extended the inviscid LSA previously done by Rayleigh [?]. Although the explanation of Rayleigh pointed that the two main causes of jet instabilities were the operation of the capillary force, whose effect is to render the jet an unstable form of equilibrium and favour its disintegration into detached drops, and those due to the dynamical character of the jet, his investigations were concentrated in liquids issued into calm air.

Tomotika's equation, in turn, was a surmise to guide newer findings, among which Meister and Scheele's [?], [?], who have developed a drop formation theory through experimental studies with 15 liquid-liquid systems and determined the jet length from which breakup occurs. Later, Kitamura [?] found experimentally that the Tomotika's theory described precisely the size of the droplets when the surrounding fluid and the main fluid moved with the same velocity. Attempts to include the relative motion of both the liquids in the LSA were conducted by Bright [?] and [?], for instance.

These pioneer studies about the stability of free jets followed the traditional approach

that defines the disturbances of the jet interface η by

$$\tilde{\eta} = ae^{i(kx-\omega t)}, \tag{1.1}$$

where x is the axial direction. Such form is initialized over the liquid surface as a result of pressure fluctuations. Weber [?], for example, solved the NS equation for a viscous liquid jet to obtain a characteristic equation which found the most unstable dimensionless growth rate and wave number being, respectively

$$\Re\{\omega\}^* = \frac{1}{2(1+3Oh_1)} \quad \text{and} \quad k^* = \frac{1}{\sqrt{2(1+3Oh_1)}}, \tag{1.2}$$

where Oh_1 is the Ohnesorge number of the dispersed phase. The Ohnesorge number relates the rate between viscous forces to inertial and surface tension forces and it is written as $Oh = \mu_{ref}/\sqrt{\rho_{ref}\sigma_{ref}L_{ref}}$, or, in a different view, as $Oh = \sqrt{We}/Re$.

Because of its unstable behaviour, a jet cannot escape the fate of breakup, which takes place in two major regimes, viz. the period of large drop formation and the spray formation. The rupture of a continuous jet in drops is motivated by a couple of applications where it occurs, such as in combustion chambers, bioprocesses, chemical emulsions, and ink jet printing. In microfluidic devices, particularly, one resorts to crossflow T-junction geometries for lubrication, enhanced mixture, among others, for which dripping regimes are intended.

The breakup stages in a gas-liquid pair are explored in Figure 5. The distance elapsed from the jet's launching station until the first drop pinches off is called *intact length*, or *breakup length*. Then, as the jet's velocity increases, the intact length tends to achieve a maximum value from which drops are formed. This point lies on somewhere between the points A and B, whereas the quasi-linear uprise marked by the points before A indicates the dripping, end of dripping and jet formation stages. Such sudden changes subsist until drops whose radii measure almost twice the jet's emerge. Between the points B and C, the drops have their radii equivalent to the jet's. Beyond the point C, droplets strip off the surface, thereby shaping a locally atomized regime. As the depth of surface dripping renders deeper, the average droplet radius become smaller so that the jet achieves the completely atomized regime after the point D, i.e. the spray regime. At this regime, the droplets' radius decreases with the inlet jet velocity.

Lin and Reitz [?] wrote a review focused on the physical mechanisms that cause the
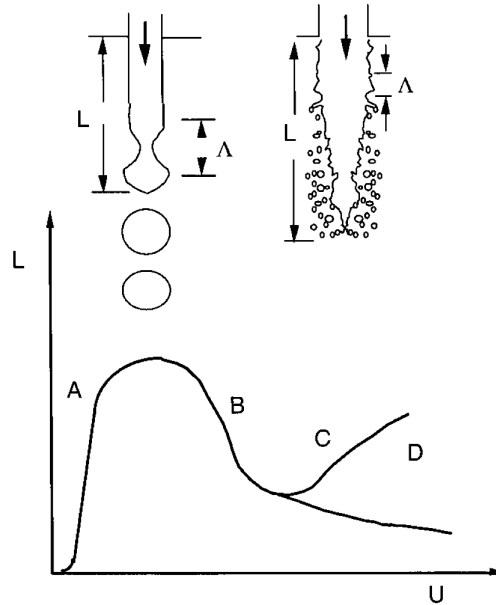
Figure 5: Diagram of the jet breakup length L vs. jet velocity U. Extracted from [?], p. 104.

onset of the jet breakup at gas-liquid interfaces. They describe four main breakup regimes corresponding to different flow properties, namely: the Rayleigh breakup regime; first wind-induced regime; second wind-induced regime and the atomization regime. By experimental observations (see Figure 6), it was verified that the breakup drop sizes are on the order of the jet diameter in the Rayleigh and first wind-induced regimes and much less in the second wind-induced and atomization regimes. Furthermore, issues about the way how pressure fluctuations around the interface from inside and outside the jet, capillary pinching with wind assistance and surface tension relate to breakup were explained. The criteria defining these breakup regimes are based on ranges of the We and Oh numbers. They are considered manifestations of convective instability and are well organized in the summary developed by [?], whose experimental results studying the Rayleigh breakup in capillary water jets have Figure 7 as an example. It describes the breakup length of a jet at its most unstable mode for different We numbers.

Richards [?] *et al.*, in their study about breakup in liquid-liquid systems asserted that the nontrivial effects due to the continuous phase outside the jet render the liquid-liquid dynamics more complicated than gas-liquid dynamics for which, most of time, the air is considered the inviscid continuous phase or hypothesized as vacuum. Such difficulties are associated to viscous, buoyancy, surface tension, inertial forces, besides jet contraction, velocity profile relaxation, and relative motion of the continuous phase. In their studies,
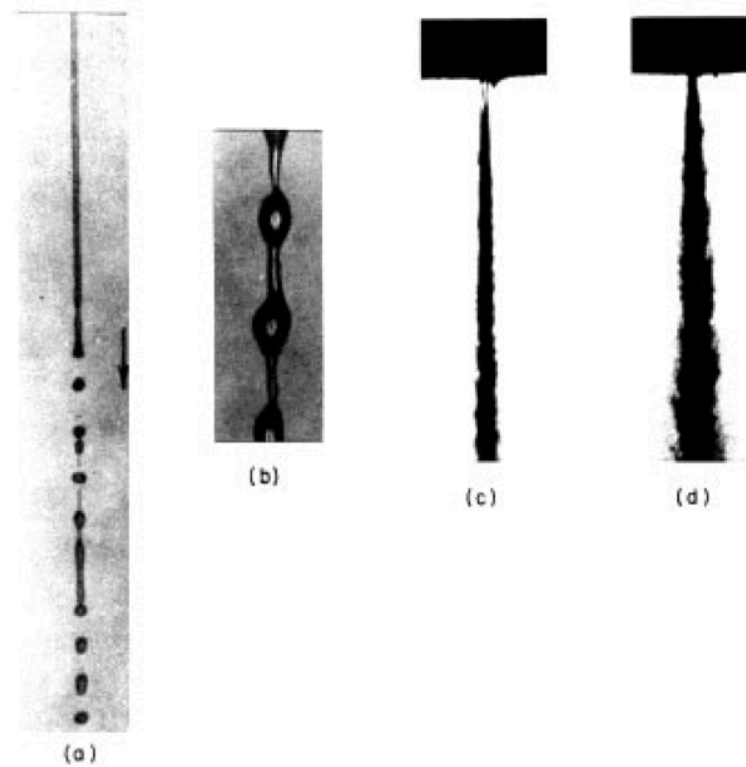
Figure 6: Experimental observation of the four breakup regimes occurring after the issuing of a round liquid jet in stagnant gas: a) Rayleigh breakup; b) first wind-induced regime; c) second wind-induced regime; d) atomization regime. Extracted from [?].
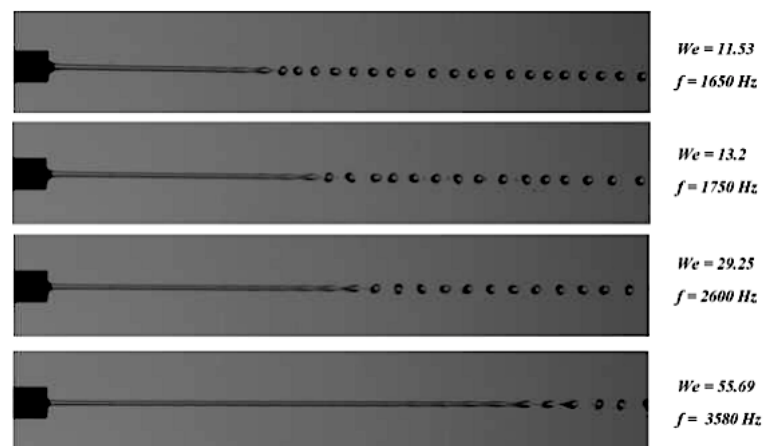
Figure 7: Breakup of a capillary water jet at the most unstable mode. Taken from [?], p. 46.

laminar flow, constant properties (e.g. viscosity, density, surface tension) and axisymmetric disturbances formed the set of hypotheses. The VOF model was applied to predict the jet length, shape, size of formed droplets through numerical simulations and comparisons with experimental data were done as well. Following a similar approach based on VOF, Homma *et al.* [?] studied breakup modes for a liquid jet injected into another immiscible liquid. They found good accordance by contrasting experimental data with their numerical code and

identified three physical breakup modes, viz. dripping, jetting with uniform droplets and jetting with nonuniform droplets, although they mentioned the limitation of their code to a certain range of parameters. These breakup modes are depicted in the diagram of Figure 8. For low injection velocities, droplets are formed periodically at the jet nozzle and no jet is observed, thereby featuring the breakup mode called *dripping*. With the increase of the jet velocity, the *jetting* mode appears. Further beyond, the jet is completely broken due to the growth of asymmetric disturbances, so that the jet intact length decreases to define the mode of *atomization.*
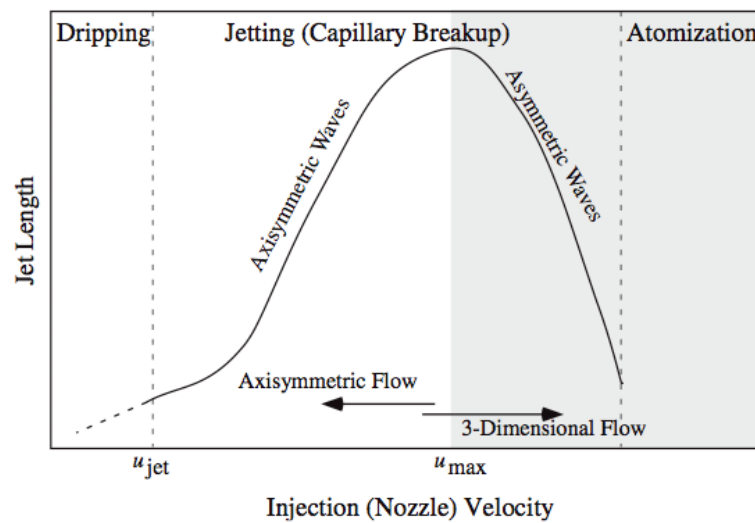
Figure 8: Breakup modes for a liquid jet injected into another immiscible liquid. Taken from [**?**].

Physical forces play a dominant role in each breakup regime, whose importance is measured by the Weber number, Reynolds number, Froude number, Mach number, density ratios, and velocity of the fluids involved. Despite of the regimes aforementioned, it is possible to find classifications even more detailed in literature. Figure 9, for instance, is a map of the primary breakup regime for liquid jets in gaseous crossflow as a function of the Weber number and the Ohnesorge number. It suggests that the Weber and Ohnesorge numbers govern breakup regime transitions according to certain situations as follow: for conditions where viscous forces are small, gasdynamic forces (or drag) on the liquid jet must be stabilized by surface tension forces, which implies that deformation and breakup regime transitions correspond to particular critical Weber numbers We_{crit} that are constant; for conditions where surface tension forces are small, on the other hand, gasdynamic forces (drag) on the liquid jet must be stabilized by liquid viscous forces, which implies that critical crossflow
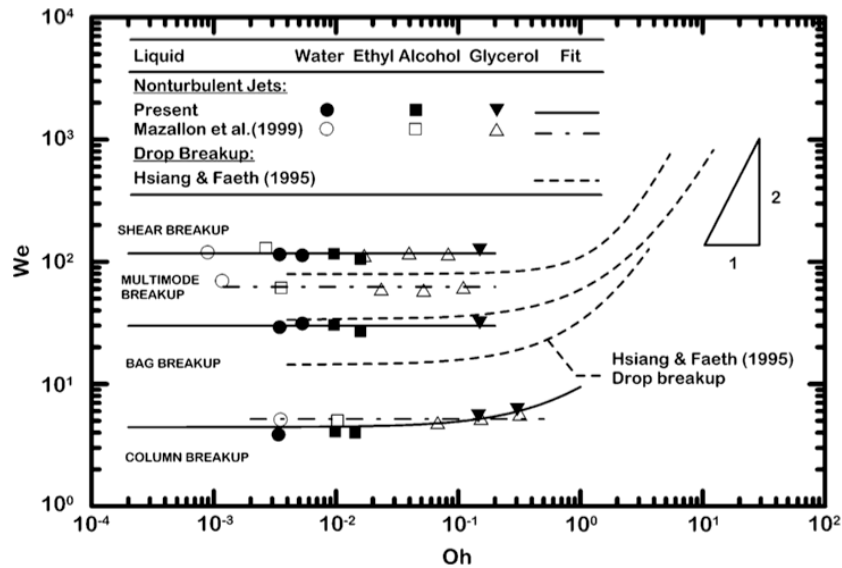
Figure 9: Primary breakup regime map for nonturbulent round liquid jets in gaseous crossflow. Extracted from [?].

Weber numbers are proportional to the square of the Ohnesorge number, i.e. $We_{crit} = \mathcal{O}(Oh^2)$. As described in the map, specific for some substances, four primary breakup regimes can be described as the Weber number increases, namely: the column (or liquid-column) breakup, bag breakup, multimode (or bag/shear) breakup and shear breakup. According to [?] in their experiments for $Oh < 1$ (small liquid viscosity), these regimes can be described as the crossflow velocity increases. These regimes are discussed briefly next. The column (or liquid-column) breakup results, at first, from the deformation of the liquid column normal to the crossflow to yield an ellipsoidal cross section which is caused by a reduction of the gas pressure near the side of the jet and ensuing acceleration of the gas over the liquid column. The drag forces due to the flattened shape of the column, in turn, enhance the tendency of the liquid to deflect toward the streamwise direction. As the liquid column deflects, thickened regions (the nodes) appear along the column and shed into drop-like structures with thinner interconnecting liquid column regions. Finally, the breakup occurs by the Rayleigh-like breakup of these filaments. As crossflow velocity increases, the bag-breakup arises after the liquid column is sufficiently flattened so that bag-like structures develop. Such bags result from the deformation of the central portion of the liquid column downstream due to the higher pressure of the stagnating gas flow on the upstream side of the flattened liquid column. With increasing distance along the liquid column, the bags grow, achieve a maximum size and begin to break beginning at their tip due to a Rayleigh-like breakup of the formed
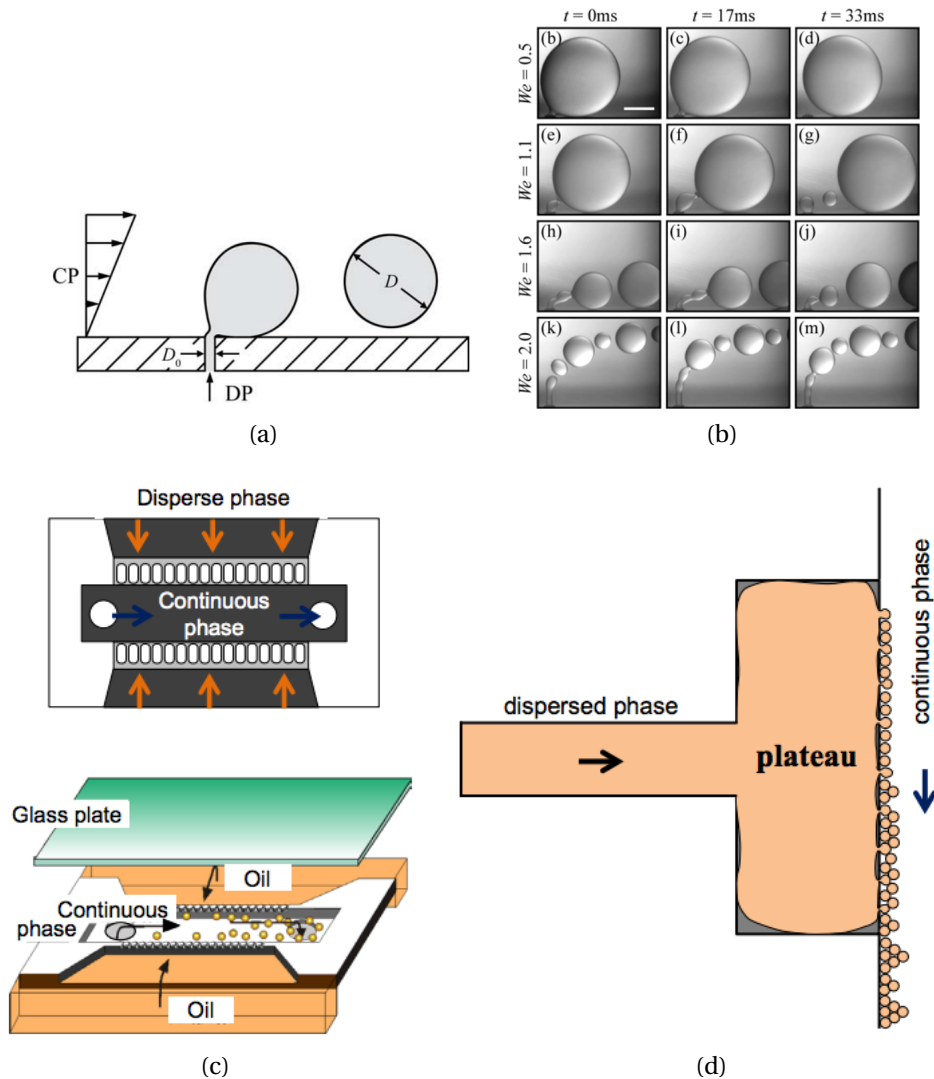
Figure 10: Crossflow membrane emulsification process: (a) diagram, (b) emulsification process (from [?]); (c) microchannel module; (d) multiple droplet generation device (from [?]).

liquid sheet as well. The multimode (or bag/shear) breakup is a complex regime which is a combination of the bag breakup and shear breakup, to be described next. In this stage, both bag-like structures, due to penetration of the liquid column, and liquid ligaments, due to the shearing of liquid from the periphery of the liquid column appear together almost at the same time. Breakup, henceforth, follows after the rupture of the bag-like and ligament structures aforementioned. Lastly, the shear breakup arises similar to the bag and multimode breakup with the largest crossflow velocity. The process begins by deflection of the liquid column toward the crossflow direction followed by distortion of the column into a flattened shape, appearing of wavelike disturbances in the upstream side of the liquid column, formation of ligaments and subsequent detachment of these ligaments. While sheet-like regions might

(a)

(b)

0 Hz, Δt = 4 ms

280 Hz, Δt = 0.2 ms

(c)
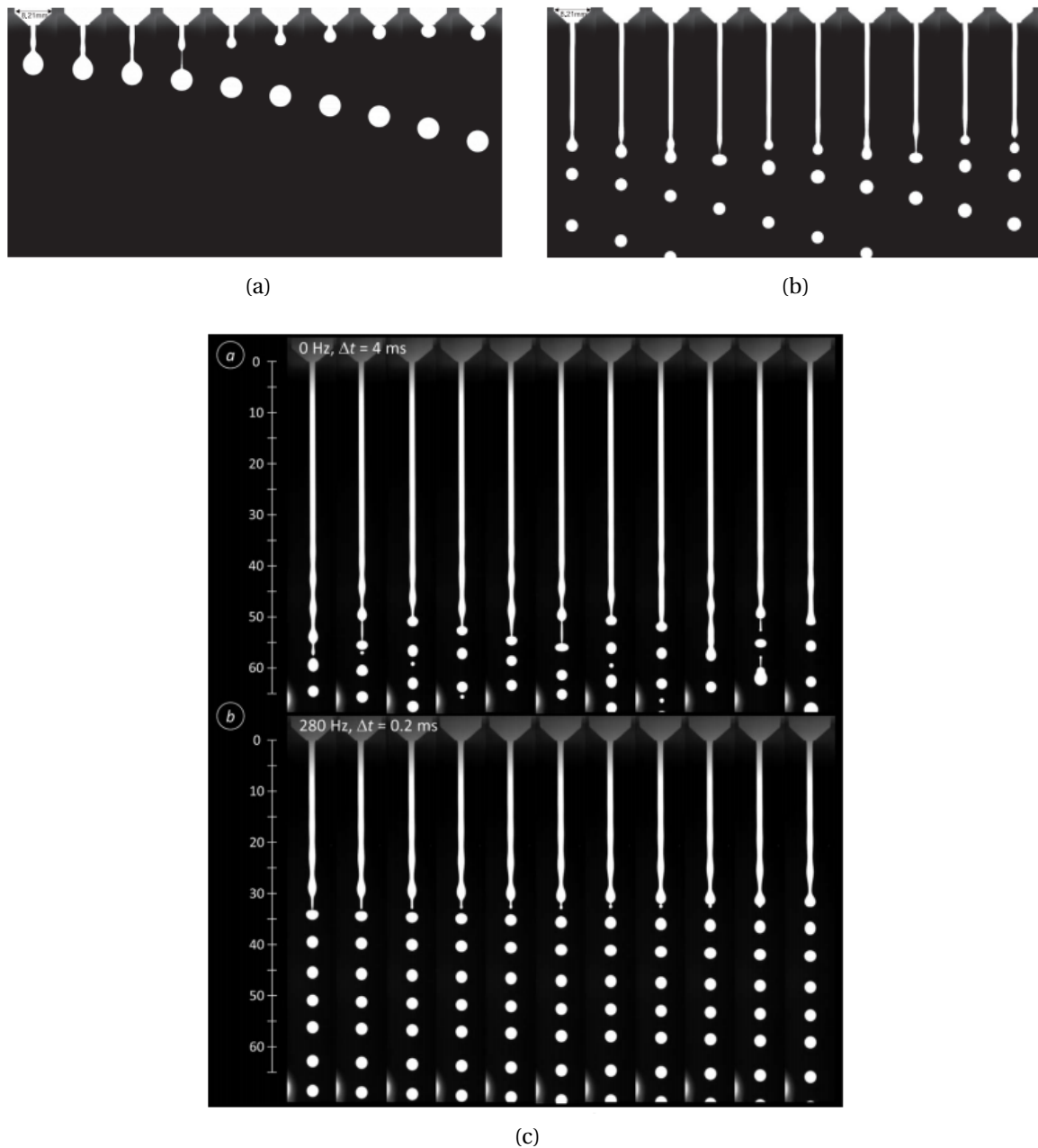
Figure 11: Drop formation and breakup of a calcia/alumina slag jet at high temperature: (a) jet formation (imagery each 5 ms), (b) developed jet (from [?]); (c) jet excited periodically (from [?]).

evolve within the ligament structures, convex bag shapes enclose them at the sides.

All things considered, it is convenient to mention some recent developments regarding drop formation in liquid-liquid systems. The performance of many modern devices in chemical processes, microfluidics and drug delivery, for instance, is closely based on crossflow shear flows along with dripping and jetting modes (see [?] and references therein). Figure 10, for instance, shows how crossflow membrane emulsification processes work. The dispersed

phase (DP) is introduced in the continuous phase (CP) by pressure through a membrane containing one or more pores. In turn, it is driven by the crossflow over the membrane's surface. The capillary breakup of jets of molten oxides (slags) at high temperatures rely on the investigation of metal production, steelmaking processes and high-precision solder printing technology. Figure 11 is an example of the formation and breakup of calcia/alumina slag jets.

1.5 Purposes of this thesis

Under the motivational aspects previously reviewed, the contribution of this thesis relies on the numerical simulation of liquid-liquid dynamics, particularly focused on the drop regime and its purposes are:

- to use an Arbitrary Lagrangian-Eulerian Finite Element Method two-phase flow code to simulate a nonturbulent liquid jet in crossflow by considering surface tension effects,

- to apply a unit cell-based model that resorts to periodic boundary conditions along with the moving frame reference technique to follow the jet, and

- to perform an analysis of the flow hydrodynamics in the primary breakup zone of drop formation based on experimental liquid-liquid pairs.

2 TWO-PHASE FLOW MODELLING: TOOL SUITE AND OVERVIEW

This thesis encompasses many different attributes as regards computational modelling. By this reason, the gist of this chapter is to accommodate an all-in excerpt about basilar concepts that will be used along the forthcoming chapters. Any order of preference is taken into account herein since each topic is viewed independently when converging to a self-content framework. Section 2.1 centers around the ALE description of movement, an useful tool to deal with flows whose interfaces are highly mobile; Section 2.2, in turn, revises some important advances in two-phase flow modelling along the years organizing a brief history of well-known numerical methods; sequentially, Section 2.3 discourses to some extent about the physicochemical behaviour of interfaces. Lastly, Section 2.4 brings up a few procedures of CAD design, pre-processing, and setting of FE meshes.

2.1 Arbitrary Lagrangian-Eulerian: a hybrid movement description

Roots of the ALE methodology stem from pioneer studies like Hirt's [?] and Chan's [?]. Nonetheless the second author proposed a generalized technique to manipulate sharp interfaces in incompressible flows, the treatment of free-surface flows and material interfaces through ALE methods continued to be envisioned by many others. Löhner [?], for instance, points out some modern examples of interactions occurring between fluids and rigid bodies, such as off-shore structures submerged in water, military torpedoes launched in the atmosphere, and rapid trains slithering through the air while entering tunnels. Generally, wetted bodies partially or totally submerged as well as deformable surfaces fall into the class of the best examples.

In the Eulerian description, an observer watches with time what happens at a fixed point in space and around it while fluid particles pass over that locus. On the other hand, in the Lagrangian description an observer is attached to a particle and travels with it undergoing all the changes concomitantly as the time elapses. Under a computational point of view, both descriptions can be used to deal with several physical problems and the reasons to opt between them should be based on suitability criteria because of their advantages and drawbacks. Next, a brief analysis of their attributes concerning the mixed ALE description will be done. We will follow substantially the writings by [?] and [?], although [?] is enlightening as a further reference and [?] a more recent text which discusses generalizaties of moving

domains.

A fundamental step to develop a CFD code is to decide which kinematic description to use. A positive point of the Lagrangian description is to allow an easy tracking of free surfaces and interfaces between different materials, but it is unskillful to follow large distortions of the computational domain without needing of frequent remeshing operations. On the other

(a)

(b)

(c)
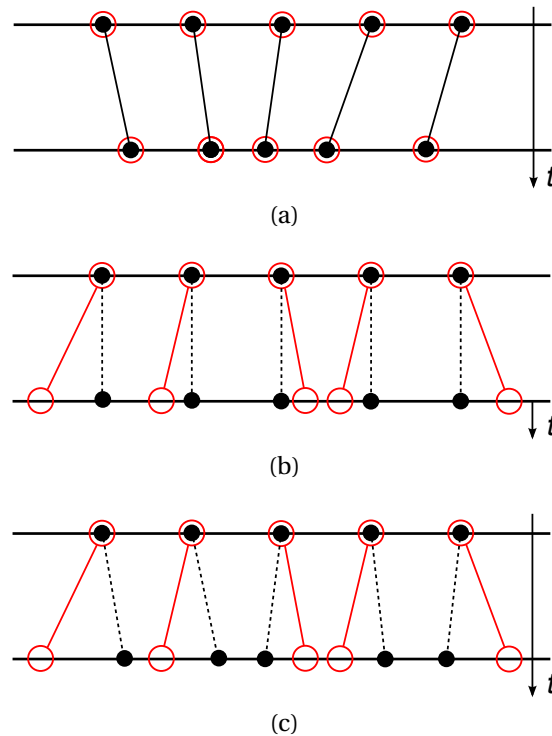
Figure 12: Scheme representing the descriptions of movement: (a) Lagrangian; (b) Eulerian; (c) ALE (hybrid).

hand, although the Eulerian description handles large distortions in the continuum motion with relative easiness, it generally requires higher computational cost to define interfaces precisely, i.e. with high resolution of the flow's details. In order to avoid the shortcomings deriving from a methodology purely Lagrangian or uniquely Eulerian, ALE/FE meshes try to grasp and combine qualities of these two methodologies to produce a better one. When the ALE description is used, some arbitrariness is permitted to the mesh nodes to move freely. Alternatively, they either remain stopped as if governed by an Eulerian fashion, or move together with the fluid, or even walk to a specified direction. These different behaviours are depicted in Figure 12. The dark points identify the mesh nodes, whereas the red circles represent material points. This freedom of movement enables a continuous rezoning functionality so that larger distortions are redressed with good resolution.

To reach its objective, the ALE methodology establishes an "intermediary" domain to

bridge an interplay between the material and spatial domains used to map the movement, which, in the ALE literature, is called the *referential domain.* These nomenclatures are suggested to follow a reasoning line, though they might slightly differ than those presented in classical books of Continuum Mechanics like [**?**], for instance. With a mathematical language, the ALE description can be deduced through the homeomorphisms represented in Figure 13 (a similar version is found in [**?**]) and ensuing didacticism. Let φ be the function that maps
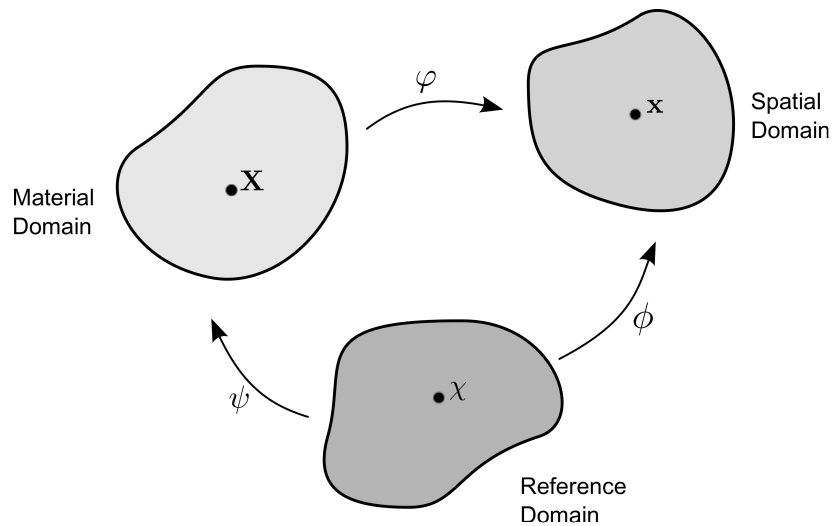
Figure 13: Mathematical representation of the descriptions of movement through homeomorphisms.

the material domain to the spatial domain defined by

$$\varphi : B_{\mathbf{X}} \times [t_0, t_f[\quad \to B_{\mathbf{x}} \times [t_0, t_f[$$
$$(\mathbf{X}, t) \qquad \mapsto \varphi(\mathbf{X}, t) = (\mathbf{x}, t).$$

Then, we can write the relation between the material domain and the spatial domain as

$$\mathbf{x} = \mathbf{x}(\mathbf{X}, t).$$

If a notation in the fashion of the Jacobian matrix for φ depending on space and time is used, a compact form to express derivatives is

$$\frac{\partial[\varphi(\mathbf{X}, t)]}{\partial(\mathbf{X}, t)} = \begin{bmatrix} \frac{\partial \mathbf{x}}{\partial \mathbf{X}} & \mathbf{v} \\ \mathbf{0}^T & 1 \end{bmatrix}, \tag{2.1}$$

where

$$\mathbf{v}(\mathbf{X}, t) = \frac{\partial \mathbf{x}}{\partial t}\bigg|_{\mathbf{X}} \tag{2.2}$$

is the *fluid velocity* and $\mathbf{0}^T$ a null row-vector.

In like manner, let ϕ be the function that maps the referential domain to the spatial domain defined by

$$\phi : B_\chi \times [t_0, t_f[\quad \to B_\mathbf{x} \times [t_0, t_f[$$
$$(\chi, t) \quad \mapsto \phi(\chi, t) = (\mathbf{x}, t).$$

A matrix notation for ϕ is also written as

$$\frac{\partial[\phi(\chi, t)]}{\partial(\chi, t)} = \begin{bmatrix} \frac{\partial \mathbf{x}}{\partial \chi} & \hat{\mathbf{v}} \\ \mathbf{0}^T & 1 \end{bmatrix}, \tag{2.3}$$

where

$$\hat{\mathbf{v}}(\chi, t) = \frac{\partial \mathbf{x}}{\partial t}\bigg|_{\chi} \tag{2.4}$$

is the *mesh velocity*.

Now, let $\boldsymbol{\Psi}$ be the function that maps the referential domain to the material domain. Differently than the aforementioned mappings, this one is described by using the inverse function as

$$\boldsymbol{\Psi}^{-1} : B_\mathbf{X} \times [t_0, t_f[\quad \to B_\chi \times [t_0, t_f[$$
$$(\mathbf{X}, t) \quad \mapsto \boldsymbol{\Psi}^{-1}(\mathbf{X}, t) = (\chi, t).$$

Similarly, a matrix notation for $\boldsymbol{\Psi}$ is written as

$$\frac{\partial[\boldsymbol{\Psi}^{-1}(\mathbf{X}, t)]}{\partial(\mathbf{X}, t)} = \begin{bmatrix} \frac{\partial \chi}{\partial \mathbf{X}} & \check{\mathbf{v}} \\ \mathbf{0}^T & 1 \end{bmatrix}, \tag{2.5}$$

where

$$\check{\mathbf{v}} = \frac{\partial \chi}{\partial t}\bigg|_{\mathbf{X}} \tag{2.6}$$

can be interpreted as the *particle velocity in the referential domain*.

From these mappings, a dependence relation among $\mathbf{v}, \hat{\mathbf{v}}$, and $\check{\mathbf{v}}$ is viewed by the

composition

$$\varphi = \phi \circ \mathbf{\Psi}^{-1}, \tag{2.7}$$

which shows a direct influence of the ALE construction on purely Eulerian or purely Lagrangian methods.

A relation among deformation gradients and velocities is better visualized when using Equation (2.1), Equation (2.3) and Equation (2.5) to write the matrix equation

$$
\begin{bmatrix} \dfrac{\partial \mathbf{x}}{\partial \mathbf{X}} & \mathbf{v} \\ \mathbf{0}^T & 1 \end{bmatrix} = \begin{bmatrix} \dfrac{\partial \mathbf{x}}{\partial \chi} & \hat{\mathbf{v}} \\ \mathbf{0}^T & 1 \end{bmatrix} \begin{bmatrix} \dfrac{\partial \chi}{\partial \mathbf{X}} & \check{\mathbf{v}} \\ \mathbf{0}^T & 1 \end{bmatrix}
$$
$$
= \begin{bmatrix} \dfrac{\partial \mathbf{x}}{\partial \chi} \dfrac{\partial \chi}{\partial \mathbf{X}} & \dfrac{\partial \mathbf{x}}{\partial \chi} \check{\mathbf{v}} + \hat{\mathbf{v}} \\ \mathbf{0}^T & 1 \end{bmatrix}. \tag{2.8}
$$

This latter identity, however, yields

$$\mathbf{v} = \hat{\mathbf{v}} + \left[\dfrac{\partial \mathbf{x}}{\partial \chi} \right] \check{\mathbf{v}}, \tag{2.9}$$

implying that the so-called *convective velocity* $\mathbf{c}$ defined by

$$\mathbf{c} : \mathbf{v} - \hat{\mathbf{v}} = \left[\dfrac{\partial \mathbf{x}}{\partial \chi} \right] \check{\mathbf{v}}, \tag{2.10}$$

works like the relative velocity between fluid and mesh. It is worth to underline that $\mathbf{c}$ should be used in the equations governing the fluid motion under an ALE approach instead of that velocity figuring in the classical forms. In a word, $\mathbf{c}$ is the essence of the ALE description.

2.2 **Short review about numerical methods**

Experimentations are by far limited to investigate all the physical effects that are crucial for a two-phase system. Testing out several conditions is highly cumbersome in terms of mounting of facilities and data analysis. For these reasons, computational modelling and numerical simulations are a feasible way to circumvent such limitation.

Many different models were devised along the last decades to deal with multiphase systems, thereby inciting the scientific community to seek methods more and more accurate

and capable of capturing the complex dynamics that springs out from these systems. Owing to their difficult modelling, the hypothesis of homogeneity is predominantly held even in the most promising methods. A brief history on the main developments concerning the computational modelling of multiphase flows based on [?] is given hereafter with particular emphasis to two-phase flows in which mobile interfaces play an important role. A point often overlooked to be noticed here is the slight difference between the *multifluid* and *multiphase* concepts. While the former is linked to the notion of different fluids, the latter is affixed to the idea of a *same* fluid, but with different phases. In other words, while a system of kind nitrogen-water is a multifluid one, a system vapour-water falls into a multiphase scope.

Boundary integral techniques started up from the 1950's as tools to simulate the Stokes flow and inviscid potential flows, whereby, later, multiphase flow simulations multiplied. Water waves, evolution of KH and RT instabilities, generation of bubbles and droplets due to coalescence, for example, are some cases to which these methods were applied. Even after five decades, some authors continued to use this approach, as reviewed by [?].

As integral techniques evolved, the MAC method appeared with the contribution of [?]. In the MAC method the fluid is identified by marker particles distributed all over the fluid region and the governing equations solved on a regular grid that covers both the fluid-filled part and the empty part of the domain. From the MAC method, new methods arose in the course of time. Replacing the marker particles with a marker function was the fundamental idea to create the VOF method, which began to be widely disclosed after [?]. The advection of the marker function, however, was a problem recognized due to the numerical diffusion resulting from working with cell-based averaging. Although the representation of the fluid interface per cell was improved, the accuracy of surface tension computation remained a problem to be tackled.

In 1992, the CSF model introduced by [?] was the ground-breaking method found to perform the calculation of surface tension, when they showed that the curvature as well as the surface tension could be computed by taking the divergence of the discrete version of the marker function. Next, [?] developed a conservative form of the CSF model. In the sequence, improvements and extensions of the VOF were developed by [?], [?], and [?], to cite only a few articles.

New approaches derived from the MAC and VOF models appeared in the decade of 1990. Unverdi and Tryggvason [?] introduced the front-tracking method in which the interface

was marked by connected marker points used to advect the material properties of the interface and compute the surface tension. This method succeeded to a large set of problems. At the same epoch, other methods came into sight, namely: the LS method by [**?**] (see also [**?**] for an extended review), soon promulgated by [**?**]; the CIP method by [**?**], and the phase-field method by [**?**], also explained in more details by [**?**] and reviewed by [**?**]. In the LS method, the interface is identified with the zero contour of a continuous level-set function. The material properties of the flow are reconstructed thereof through a marker function constructed from the level-set function. This approach opposes to the VOF's, in which a discontinuous marker function is advected with the flow. Differently, the CIP method seeks to describe the transition at the interface by a cubic polynomial. The phase-field method modifies the governing equations so that the region between the fluids can be described by a thermodynamically consistent way.

As seen, many methods were devised to face the numerical difficulties arising in the multiphase universe. In spite of their characteristics, the so-called "one-fluid" formulation has been being featured in modern codes because of its ability to treat the different fluids or phases as a unique domain, a reason why it is also employed in this thesis. With this in mind, it was preferred to postpone the discussion of this topic in order to introduce it, especially, on the pages devoted to the equations roster in Section 3.1.

2.3   Interface and surface tension

The very thin region created when two phases of matter come into contact is called interface. To be maintained, we should suppose that both the phases have different properties, which, at molecular level, work oppositely one another to retain the physical equilibrium. By considering the three states of the matter – plasma interfaces are not discussed here –, the possible types of interfaces are: gas-liquid, gas-solid, liquid-liquid, liquid-solid and solid-solid. Owing to the proposals of this thesis, we will shorten the essay to comment on fluids only. According to Adamson [**?**], a general prerequisite for the stable existence of an interface between two phases is that the free energy of formation of the interface be positive. Otherwise, the interface would be expanded and dispersed, thereby leading the phases to mix. In turn, any change provoked by one phase is felt by the other while they are separated by the interface. As an illustration, Figure 14 (adapted from [**?**]) clarifies the molecular imbalance observed near an arbitrary interface of a gas-liquid system. The color gradient in the interstice between the shaded stems is an analogy to the density jump at the interface, as it would occur

for another physical quantity, whereas η measures the normal distance to the interface.
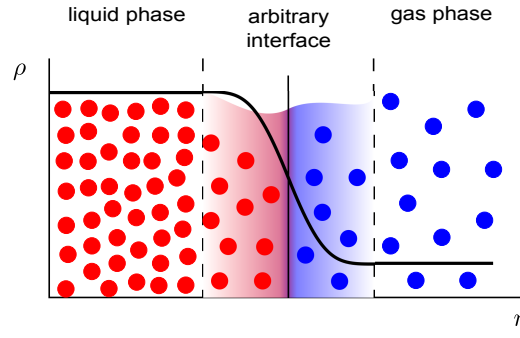
Figure 14: An outlook of the molecular imbalance in the surroundings of an arbitrary gas-liquid interface.

More complex situations occur when three or more phases give rise to multiple interfaces. This is the case of two fluids that, beyond being in contact each other, rest together upon a solid wall as to create a third interface, for instance. With the development of new technologies guided by multiphase systems, such class of problems frequently correspond to big challenges in industrial, chemical and biological applications. This scenario is responsible to wage resources in studies about interface phenomena. A more accurate glimpse on interface and surface tension are given next.

We can represent the interface between two fluids through an equation that describes a surface ζ immersed in space. In the most general case, this surface is assumed to vary with the time. Hence, it can be written by a relation given by $\zeta(\mathbf{x}, t) = 0$. If we consider that ζ is moving with velocity $\mathbf{v}$, each of its points undergoes an infinitesimal displacement $\delta\mathbf{x} = \mathbf{v}\delta t$ after a time interval δt so that the new equation describing ζ is written as

$$\zeta(\mathbf{x} + \delta\mathbf{x}, t + dt) = \zeta(\mathbf{x} + \mathbf{v}\delta t, t + dt) = 0. \tag{2.11}$$

But, with $\mathbf{v} = (v_x, v_y, v_z)$, $\delta\mathbf{x} = (v_x\delta t, v_y\delta t, v_z\delta t)$ reads for the displacement of each coordinate. By applying a Taylor expansion on two variables (space and time), we can linearly approximate any change of ζ. Therewith, we are conducted to a material displacement

$$\zeta(x + \delta x, y + \delta y, z + \delta z, t + \delta t) = \zeta(x, y, z) + \delta x\frac{\partial\zeta}{\partial x} + \delta y\frac{\partial\zeta}{\partial y} + \delta z\frac{\partial\zeta}{\partial z} + \delta t\frac{\partial\zeta}{\partial t}, \tag{2.12}$$

or

$$\zeta(x + \delta x, y + \delta y, z + \delta z, t + \delta t) = \zeta(x, y, z) + (v_x\delta t)\frac{\partial\zeta}{\partial x} + (v_y\delta t)\frac{\partial\zeta}{\partial y} + (v_z\delta t)\frac{\partial\zeta}{\partial z} + \delta t\frac{\partial\zeta}{\partial t}, \tag{2.13}$$

which gives rise to the material derivative applied to ζ

$$\frac{D\zeta}{Dt} = \frac{\zeta(x+\delta x, y+\delta y, z+\delta z, t+\delta t) - \zeta(x,y,t)}{\delta t} = v_x\frac{\partial\zeta}{\partial x} + v_y\frac{\partial\zeta}{\partial y} + v_z\frac{\partial\zeta}{\partial z} + \frac{\partial\zeta}{\partial t}, \qquad (2.14)$$

provided that δt is assumed small and the linearity assumption used. Hence, the well-known compact form of the operator $\frac{D}{Dt}$ applied to ζ is written as

$$\frac{D\zeta}{Dt} = \frac{\partial\zeta}{\partial t} + \mathbf{v}\cdot\nabla\zeta. \qquad (2.15)$$

This derivation comes after [**?**]. *De facto*, as registered by [**?**], the condition

$$\frac{D\zeta}{Dt} = 0, \quad \text{at} \quad \zeta = 0 \qquad (2.16)$$

is the so-called *kinematic boundary condition*, which says that if a particle is on the interface at a particular time t_0 it will be always there for all $t > t_0$ since the interface is a material surface.

Interfaces that are sufficiently mobile to assume an equilibrium shape (e.g. meniscus, drops and thin films) stick to the matter of *capillarity*, a vein of Thermodynamics. It deals with the macroscopic and statistical behaviour of interfaces rather than with the details of the molecular structure. Notwithstanding, the concept of surface tension, although surrounded by the physical sense of attractive and repulsive forces, plays a relevant role for the former topic.

In [**?**], it is discussed that the surface tension can be interpreted dually. On one hand, as a free energy per unit area; on the other hand, as a force per unit length. Furthermore, the author declares that the name *surface free energy* is preferable to *surface tension* in view of a misunderstanding to which we might come across when interpreting its physical meaning. However, despite of conceptual divergences, both of the aforementioned terms are used interchangeably. Figure 15 depicts an infinitesimal element dA as well as the tangential distribution of the surface tension σ upon it.

In this thesis, effects of contaminants or surfactants due to gradients of surface tension – i.e., Marangoni effects – are absent. In this manner, σ is uniform along any curve immersed in the surface. The blue dashed curves intersecting at the center of the infinitesimal element are special, since they determine the principal radii of curvatures R_1, R_2 when the interface
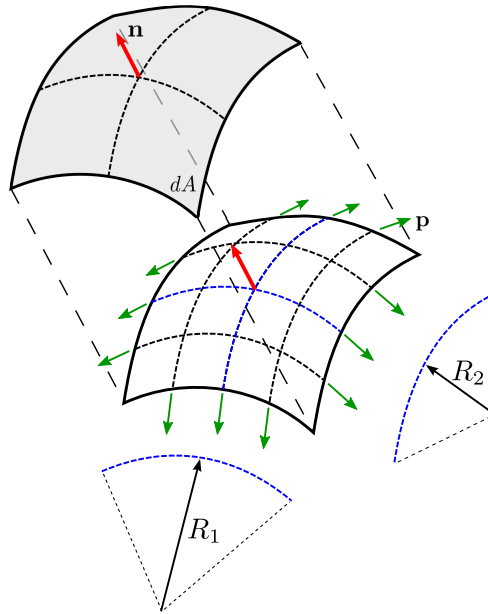
Figure 15: Uniform distribution of the surface tension over an infinitesimal area and principal radii of curvature.

slips away from the equilibrium after being perturbed locally. The unit vector $\mathbf{n}$ helps to quantify curvatures and guides the determination of the capillary pressure taking place at the interface.

Despite of the physical sight about the surface tension, the mechanical point of view is equally enlightening. According to [?], it can be shown that the force on the edge of the element in Figure 15 is written as $\mathbf{T}_A^\sigma \cdot \mathbf{p}$, where $\mathbf{T}_A^\sigma$ is the surface tension tensor and $\mathbf{p}$ the vector normal to the edge of dA in a tangent plane. Additionally, σ is an eigenvalue of $\mathbf{T}_A^\sigma$ so that

$$\mathbf{T}_A^\sigma \mathbf{p} = \sigma \mathbf{p} \;\Rightarrow\; \mathbf{T}^\sigma = \sigma \mathbf{I}_A. \tag{2.17}$$

To put another way, since $\mathbf{n}$ can be obtained by the cross product between the two orthonormal tangent vectors $\mathbf{t}_1, \mathbf{t}_2$, it is found that

$$\mathbf{T}_A^\sigma = \sigma (\mathbf{t}_1 \otimes \mathbf{t}_1 + \mathbf{t}_2 \otimes \mathbf{t}_2). \tag{2.18}$$

The force on the element dA is the integral of the "pull" on its boundary ∂A (i.e., the union of its edges), which is given by

$$\delta \mathbf{F}_\sigma = \oint_{\partial A} \mathbf{T}_A^\sigma \mathbf{p} \, dl = \int_A \nabla_A \cdot \mathbf{T}_A^\sigma \, dA, \tag{2.19}$$

whence, after taking the limit up to a point, the surface force per unit area renders

$$\mathbf{f} = \nabla \cdot \mathbf{T}_A^{\sigma} = \nabla_A \cdot \sigma \mathbf{I}_A = \sigma \nabla_A \cdot \mathbf{I}_A + \mathbf{I}_A \cdot \nabla_A \sigma. \tag{2.20}$$

Thenceforth, it is shown that $\nabla_A \cdot \mathbf{I}_A = \kappa \mathbf{n}$, implying the expression

$$\mathbf{f} = \sigma \kappa \mathbf{n} + \nabla_A \sigma, \tag{2.21}$$

in which the second term corresponds to the presence of Marangoni effects, already assumed to be absent here. Hence, it remains

$$\mathbf{f} = \sigma \kappa \mathbf{n}. \tag{2.22}$$

2.4 **Meshing art and generalities**

Mesh generation is the heartwood of the pre-processing stage of any computational code. Along the times, a plethora of softwares as well as algorithms to create grids suitable to complex geometries were developed, thus glossing a scenario increasingly compared to a true craftwork. Generally, FE meshes can be created from arbitrary geometries drawn by CAD softwares, such as the best-known commercial packages for engineering purposes AutoCAD® and SolidWorks®. Currently, CFD tools like Ansys Fluent® and Comsol Multiphysics® - the latter having diverse FE resources - bring built-in CAD capabilities and are engaged to gather all the stages of simulation into an integrated tool. On the other hand, free softwares devoted to do similar operations are also available. Some tools, such as TRIANGLE [?], TETGEN [?], and GMSH [?] were invaluable for this thesis, from which the meshes were generated. Despite of that, this section aims to present some descriptive tools useful to pave the two-phase framework which all the remain material will be subjected to.

Preliminarily, as a general example, let $\Omega \subset \mathbb{R}^m$, $m = 2, 3$ be a domain and Γ its boundary, both of which defined as

$$\begin{aligned} \Omega \quad &:= \quad \Omega^1 \cup \Omega^2, \quad \text{where} \quad \Omega^1 = \bigcup_{g=1}^{nb} \Omega_g^1, \quad \text{and} \\ \Gamma \quad &:= \quad \Gamma^1 \cup \Gamma^2, \quad \text{where} \quad \Gamma^1 = \bigcup_{g=1}^{nb} \Gamma_g^1, \quad \Gamma^2 = \Gamma_D \cup \Gamma_P \end{aligned}$$

respectively, where the subscripts $1, 2$ indicate, in this sequence, the dispersed and continuous phase of a two-fluid flow, Γ_D (Γ_P) the Dirichlet (periodic) portion of Γ^2, and nb the number of elements of the dispersed phase. Also, call $\mathbf{n}_{12}$ and $\mathbf{n}_{2,D}$ ($\mathbf{n}_{2,P}$) unit normal vectors pointing from Ω^1 to Ω^2 and outward Γ_D (Γ_P), respectively. Depending on the flow to be analyzed, Γ^1 may be made up by impermeable solid walls, open boundaries, or inlets, for instance, while each Γ_g^2 may represent bodies with mobile interfaces, such as gas bubbles or liquid drops not coalescing one with another. Particularly, Γ_P will be ascribed suitably with Neumann conditions according to a FE sense – discussed in Chapter 5. Figure 16 sketches a typical domain as described above for a two-phase flow formulation.
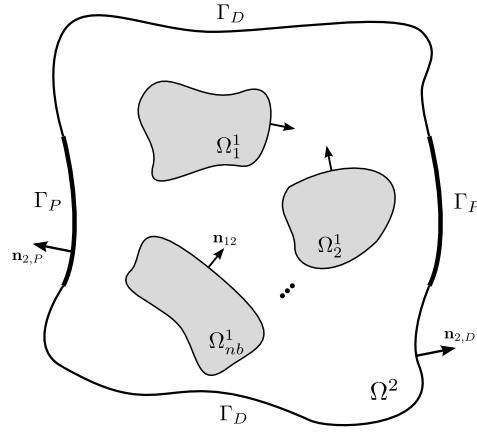
Figure 16: Generalized domain including periodic boundaries for a two-phase flow modelling.

Given a tessellation $\mathcal{T}_h$ of Ω, each simplex $T \in \mathcal{T}_h$ here either is a triangle ($m = 2$) or a tetrahedron ($m = 3$) with vertices $\mathbf{x}_j$, $1 \le j \le m+1$, obeying the classical requirements for a finite element [?], [?]. To describe the mesh structure used to establish the two-fluid nature studied here, a simplistic mathematical description is introduced based on families of discrete parts. Thenceforth, we define

$$\mathcal{T}_{h_1}^{\Gamma^1} := \{T \in \mathcal{T}_h;\ T \in \text{interface}\}, \tag{2.23}$$

$$\mathcal{T}_{h_2}^{\Gamma^2} := \{T \in \mathcal{T}_h;\ T \in \text{convex hull}\}, \tag{2.24}$$

$$\mathcal{T}_{h_\Gamma}^{\Gamma} := \mathcal{T}_{h_1}^{\Gamma^1} \cup \mathcal{T}_{h_2}^{\Gamma^2} \tag{2.25}$$

$$\mathcal{T}_h^{\Omega^1} := \{T \in \mathcal{T}_h;\ \mathring{T} \subset \Omega^1\}, \quad \rightsquigarrow \blacksquare \text{(elements)}, \tag{2.26}$$

$$\mathcal{T}_h^{\Omega^2} := \{T \in \mathcal{T}_h;\ \mathring{T} \subset \Omega^2\}, \quad \rightsquigarrow \square \text{(elements), and} \tag{2.27}$$

$$\mathcal{T}_h^{\Omega} := \mathcal{T}_h^{\Omega^1} \cup \mathcal{T}_h^{\Omega^2}, \tag{2.28}$$

as mesh subsets. The symbol "⤳" is used in Figure 17 for a graphical representation of element families sharing an interface in a two-dimensional mesh. Despite of these mathematical definitions, the computational mesh is stored into two data structures only, viz. the *area/volume mesh* $\mathcal{T}_h^\Omega$, which accounts for an interior discretization and the *line/surface mesh* $\mathcal{T}_{h_\Gamma}^\Gamma$, which discretizes convex hulls and interfaces. Different levels of adaptive refinement h, h_1, h_2 can be chosen separately for volumes, interfaces and boundaries according to the flow conditions.

Since an interface is traced by edges or faces of the own mesh elements, a sharp thickness is achieved satisfactorily. Therefore, this construction evinces a kind of front-tracking method in which such an interface is identified by evaluating a nodal Heaviside function $H(\mathbf{x})$ over the elements belonging to $\mathcal{T}_{h_1}^{\Gamma^1}$. As pointed out by [**?**], it turns out that the abrupt transition of a property ϕ across the interface can be smoothed with by means of the interpolation

$$\phi(\mathbf{x}) = \phi^1 H(\mathbf{x}) + \phi^2 (1 - H(\mathbf{x})), \quad \forall \mathbf{x} \text{ of } T \in \mathcal{T}_h, \quad \phi^i = \phi|_{\Omega^i}, \, i = 1, 2. \tag{2.29}$$

Besides, we set forth

$$H(\mathbf{x}_j) := \begin{cases} 0, & \text{if } \mathbf{x}_j \in \mathcal{T}_h^{\Omega^2} \cup \mathcal{T}_{h_2}^{\Gamma^2} \\ 0.5, & \text{if } \mathbf{x}_j \in \mathcal{T}_{h_1}^{\Gamma^1} \\ 1, & \text{if } \mathbf{x}_j \in \mathcal{T}_h^{\Omega^1}. \end{cases} \tag{2.30}$$

for the nodal evaluation. Figure 17 is an overview of elements comprising a neighbourhood of interface highlighting the effect of the interpolation given by 2.29.
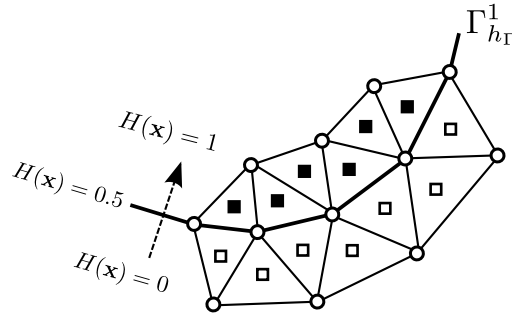
Figure 17: Mesh elements comprising the region around the discrete interface between the fluids and effect of transition caused by interpolation with the Heaviside function.

All things considered, the meshing process for the desired two-phase flow configu-

ration is now illustrated in Figure 18 in order to single out how the elements are connected in such a way to create zero-thickness interfaces. The model encompasses three spherical bodies (e.g. bubbles, or drops) dispersed into a medium that is confined inside a truncated microchannel. Such a setup is suitable to study, for instance, the dynamics of bubbles in microscale devices, the breakup and pre-atomization regimes ocurring in liquid jets as well as the study of bubble interaction under PBC as will be reported later in Chapter 5. In the same figure, at the top, the quarter of the cylindrical geometry is depicted after the cut by two mutually perpendicular planes to the axis of revolution. As can be seen by the plotting of the Heaviside function $H(\mathbf{x})$, the whole domain as well as the interface locus are well represented by the mesh elements. At the bottom, the overview of the entire surfaces is drawn. An additional example for a model of a long capsule-shaped bubble typically encountered in two-phase slug flow regimes is depicted in Figure 19, where $H(\mathbf{x})$ plays the role as marker function.
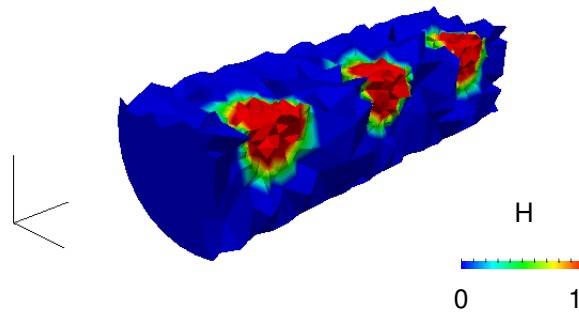
(a)
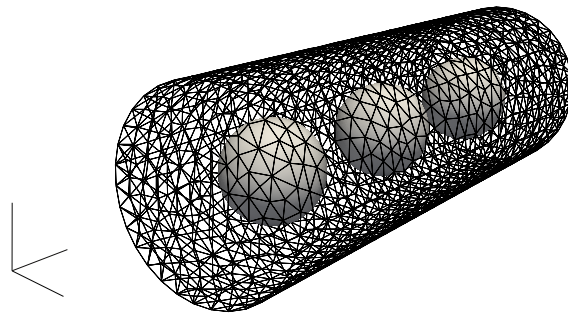
(b)

Figure 18: 3D mesh for an arbitrary two-phase flow configuration containing three dispersed spherical elements confined into a microchannel (a) Heaviside function marking the bulk region, interface locus and inner phase; (b) overview of the equally-spaced spherical bodies in the microchannel.
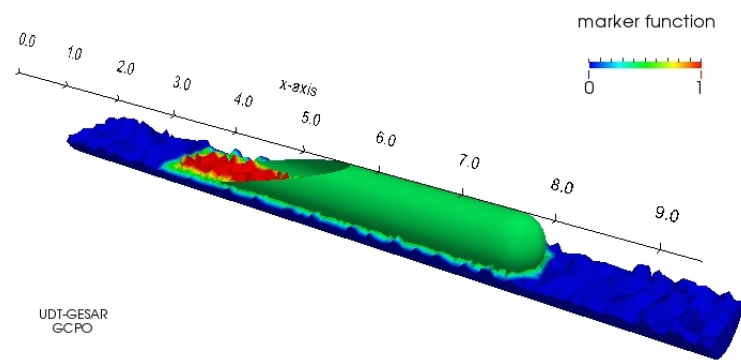
 Figure 19: 3D mesh for a long capsule-shaped bubble typically encountered in two-phase slug flow configurations taken from [?].

3   GOVERNING EQUATIONS

3.1   **Principles**

Conservation laws have utter relevance before any thorough study because they gather a set of fundamental hypotheses that drive the behaviour of a physical system. This section presents these main conservation laws and the equations governing the movement of fluids according to the Continuum Mechanics [**?**]. Integral forms are the starting point in head to a more suitable set of partial differential equations. A summarized writing, however, is preferred instead of a detailed scrutiny upon each principle.

3.1.1   Mass conservation

The terminology *body* is used to specify any limited portion of space with mass m. If we call such body B, ρ_t its density associated with the time, then,

$$m(B) = \int_B \rho_t \, dV. \tag{3.1}$$

Moreover, let ∂B be the boundary of B, $\mathbf{n}$ a unit normal vector pointing outward and $\mathbf{v}$ the velocity field of the fluid. By invoking the Divergence Theorem, it holds the equation

$$\int_B \nabla \cdot (\rho \mathbf{v}) \, dV = \int_{\partial B} \rho \mathbf{v} \cdot \mathbf{n} \, dA. \tag{3.2}$$

For each point $\mathbf{x} \in B$ at a particular time t, we define

$$\int_B \frac{\partial}{\partial t} \rho(\mathbf{x}, t) \, dV = \frac{d}{dt} \int_B \rho(\mathbf{x}, t) \, dV. \tag{3.3}$$

By combining Equations (3.2) and (3.3), we write the *Principle of Mass Conservation* for a control volume as

$$\frac{d}{dt} \int_B \rho(\mathbf{x}, t) \, dV = -\int_{\partial B} \rho(\mathbf{x}, t) \mathbf{v}(\mathbf{x}, t) \cdot \mathbf{n}(\mathbf{x}) \, dA. \tag{3.4}$$

To put another way, Equation (3.4) declares that the mass production rate inside B is numerically equal to the net mass flux flowing out its boundary. Furthermore,

$$\frac{\partial \rho}{\partial t} + \nabla \cdot (\rho \mathbf{v}) = 0, \tag{3.5}$$

holds and it is the *Continuity Equation.* By using the vectorial identity $\nabla \cdot (\rho \mathbf{v}) = \mathbf{v} \cdot \nabla \rho + \rho \nabla \cdot \mathbf{v}$, Equation (3.5) is recast to

$$\frac{\partial \rho}{\partial t} + \mathbf{v} \cdot \nabla \rho + \rho (\nabla \cdot \mathbf{v}) = 0. \tag{3.6}$$

A simplified version of the continuity equation is obtained when one assumes that the density is constant in time, thus evoking the incompressibility hypothesis $\frac{D\rho}{Dt} = 0$. Consequently, Equation (3.6) is reduced to the kinematic restriction

$$\nabla \cdot \mathbf{v} = 0, \tag{3.7}$$

3.1.2   Linear momentum

When a body B moves over a continuum, interactions among its particles as well as between B and its surroundings can take place as distinct manifestations of forces. This system of forces acting upon B can be written, in turn, as a pair $(\mathbf{s}, \mathbf{b})$ of functions, such that

$$\mathbf{s} : \mathcal{N} \times \mathcal{X} \longrightarrow \mathbb{R}^m \quad \mathbf{b} : \mathcal{X} \longrightarrow \mathbb{R}^m$$

$\mathbf{s}(\mathbf{n}, \mathbf{x}, t)$, for $\mathbf{n} \in \mathcal{N}$, $\mathbf{x} \in \mathcal{X}$ at the time t are called *surface forces*, whereas $\mathbf{b}(\mathbf{x}, t)$ are named *body forces*. By assuming that the state of stress at a point $\mathbf{x}_\partial \in \partial B$ is given by the symmetric tensor $\mathbf{T}_{\mathbf{x}_\partial}$, the total surface force on B is given by

$$\int_{\partial B} \mathbf{T}_{\mathbf{x}_\partial} \cdot \mathbf{n} \, dA, \tag{3.8}$$

for $\mathbf{n}$ unitary placed at $\mathbf{x}_\partial$ and pointing outward B. Furthermore, since $\mathbf{b}$ acts upon the interior of B, the body forces summed up correspond to

$$\int_B \mathbf{b} \, dV. \tag{3.9}$$

Similarly to the previous section, the net flux of momentum to be considered renders

$$\int_{\partial B} (\rho \mathbf{v} \otimes \mathbf{v}) \cdot \mathbf{n} \, dA. \tag{3.10}$$

Put together, these forces correspond to the balance of momentum in B, which corresponds to the equation

$$\int_B \frac{\partial}{\partial t}(\rho \mathbf{v}) \, dV = -\int_{\partial B} (\rho \mathbf{v} \otimes \mathbf{v}) \cdot \mathbf{n} \, dA + \int_{\partial B} \mathbf{T}_{\mathbf{x}_\partial} \cdot \mathbf{n} \, dA + \int_B \mathbf{b} \, dV. \tag{3.11}$$

Frequently, $\mathbf{b} = \rho \mathbf{g}$, associating to the gravitational field $\mathbf{g}$. Now, again through the Divergence Theorem, we obtain, by taking the gravitational field into account,

$$\int_B \frac{\partial}{\partial t}(\rho \mathbf{v}) \, dV = -\int_B \nabla \cdot (\rho \mathbf{v} \otimes \mathbf{v}) \, dV + \int_B \nabla \cdot \mathbf{T}_{\mathbf{x}_\partial} \, dV + \int_B \rho \mathbf{g} \, dV. \tag{3.12}$$

In virtue of treating B infinitesimally, a differential form valid all over stemming from Equation (3.12) is given by

$$\frac{\partial}{\partial t}(\rho \mathbf{v}) + \nabla \cdot (\rho \mathbf{v} \otimes \mathbf{v}) = \nabla \cdot \mathbf{T}_{\mathbf{x}_\partial} + \rho \mathbf{g}. \tag{3.13}$$

On the other hand, through the identities

$$\nabla \cdot (\rho \mathbf{v} \otimes \mathbf{v}) = (\rho \mathbf{v}) \nabla \mathbf{v} + \mathbf{v} \nabla \cdot (\rho \mathbf{v}) \tag{3.14}$$

and

$$\frac{\partial}{\partial t}(\rho \mathbf{v}) = \frac{\partial \rho}{\partial t} \mathbf{v} + \rho \frac{\partial \mathbf{v}}{\partial t}, \tag{3.15}$$

Equation (3.13) renders

$$\rho \left(\frac{\partial}{\partial t} + \mathbf{v} \cdot \nabla \right) \mathbf{v} + \mathbf{v} \left(\frac{\partial \rho}{\partial t} + \nabla \cdot (\rho \mathbf{v}) \right) = \nabla \cdot \mathbf{T}_{\mathbf{x}_\partial} + \rho \mathbf{g}. \tag{3.16}$$

Though, Equation (3.5) enforces $\frac{\partial \rho}{\partial t} + \nabla \cdot (\rho \mathbf{v}) = 0$, whereby

$$\rho \left(\frac{\partial \mathbf{v}}{\partial t} + \mathbf{v} \cdot \nabla \mathbf{v} \right) = \nabla \cdot \mathbf{T}_{\mathbf{x}_\partial} + \rho \mathbf{g} \tag{3.17}$$

is a final form for the momentum equation.

Theoretically, it is shown that, for Newtonian fluids – to which we report herein –, $\mathbf{T}$ is assumed to be a linear function of the rate of strain, namely,

$$\mathbf{T} = (-p + \lambda \nabla \cdot \mathbf{v})\mathbf{I} + 2\mu \mathbf{D}, \tag{3.18}$$

where the subscript $\mathbf{x}_{\partial}$ was dropped out for readability. Above, p is the pressure, $\mathbf{I}$ is the identity tensor, μ is the viscosity, and $\mathbf{D} = \frac{1}{2}\left(\nabla \mathbf{v} + \nabla \mathbf{v}^{T}\right)$ is the deformation tensor. λ is the coefficient of second viscosity which, by the Stokes' law, will be determined by assuming a zero bulk viscosity, i.e., $\lambda + \frac{2}{3}\mu = 0$. Thereupon, Equation (3.17) rewritten as

$$\rho \frac{D\mathbf{v}}{Dt} = -\nabla p + \nabla \cdot \left[\mu \left(\nabla \mathbf{v} + \nabla \mathbf{v}^{T}\right)\right] - \nabla \left(\frac{2}{3}\mu \nabla \cdot \mathbf{v}\right) + \rho \mathbf{g} \tag{3.19}$$

results in the Navier-Stokes equation. Since we will deal with incompressible flows only, Equation (3.7) allows us to attain the simplified form

$$\rho \frac{D\mathbf{v}}{Dt} = -\nabla p + \nabla \cdot \left[\mu \left(\nabla \mathbf{v} + \nabla \mathbf{v}^{T}\right)\right] + \rho \mathbf{g} \tag{3.20}$$

At this point, remember that Equation (3.20) should be written considering the ALE referential according to the subject-matter of Section 2.1. In effect, by inserting the convective velocity (cf. Equation (2.10)) into Equation (3.20) and rewriting the advection term of the material derivative, we obtain the ALE form for the momentum equation

$$\rho \left(\frac{\partial \mathbf{v}}{\partial t} + \mathbf{c} \cdot \nabla \mathbf{v}\right) = \rho \left(\frac{\partial \mathbf{v}}{\partial t} + (\mathbf{v} - \hat{\mathbf{v}}) \cdot \nabla \mathbf{v}\right) = -\nabla p + \nabla \cdot \left[\mu \left(\nabla \mathbf{v} + \nabla \mathbf{v}^{T}\right)\right] + \rho \mathbf{g} \tag{3.21}$$

3.1.3 Advection-diffusion equation

Plentiful phenomena involving the concentration of species occur in nature under the form of binary mixtures or multicomponent systems. Many of them are described by advection-diffusion-reaction equations that take into account all the complex effects arising from the interaction among those substances in space and time. Let us consider Ψ the mass concentration of an arbitrary chemical species ϕ which is distributed over a body B. The

principle of conservation for such chemical species over B is applied as

$$\int_B \frac{\partial \Psi}{\partial t}\, dV = -\int_{\partial B} \mathbf{j} \cdot \mathbf{n}\, dA + \int_B f(CK)\, dV, \tag{3.22}$$

i.e. the rate of concentration of the chemical species in B is equal to the net flux of concentration $\mathbf{j}$ crossing the body's boundary added by the rate of mass production or destruction as a function of the chemical kinetics $f(CK)$. Here, we will consider $f(CK)$ identically zero. Note, on the other hand, that this equation will be introduced here for future testing purposes only concerning the transport of a scalar passive. Hence, any coupling with the momentum equation is considered.

Thenceforth, by applying the Divergence Theorem to the l.h.s. of Equation (3.22), we obtain

$$\int_B \frac{\partial \Psi}{\partial t}\, dV = -\int_B \nabla \cdot \mathbf{j}\, dV, \tag{3.23}$$

whereof

$$\frac{\partial \Psi}{\partial t} = -\nabla \cdot \mathbf{j}. \tag{3.24}$$

By means of the Fick's first law of diffusion, viz. $\mathbf{j} = -\varrho \nabla \Psi$, the previous equation renders

$$\frac{\partial \Psi}{\partial t} - \varrho \nabla^2 \Psi, \tag{3.25}$$

for a mass diffusivity ϱ. Additionally, to have a full unsteady description of the diffusive process during the transport of concentration due to a carrying fluid, the convective variation of concentration should be included in Equation (3.25), thus conducting it to

$$\frac{\partial \Psi}{\partial t} + \mathbf{v} \cdot \nabla \Psi - \varrho \nabla^2 \Psi = 0, \tag{3.26}$$

or, concisely, in the sense of the material derivative,

$$\frac{D\Psi}{Dt} = \varrho \nabla^2 \Psi. \tag{3.27}$$

In order to get the dimensionless form of Equation (3.27), the Peclét number

$$Pe = \frac{U_{ref}L_{ref}}{\varrho_{ref}},$$
(3.28)

measuring the relation between the advective transport rate and the diffusive transport rate of Ψ is segregated into the product

$$Pe = ReSc, \quad Sc = \frac{\nu_{ref}}{\varrho_{ref}}$$
(3.29)

to produce

$$\frac{D^*\Psi^*}{D^*t^*} = \frac{1}{ReSc}\nabla^{*2}\Psi^*,$$
(3.30)

or, by removing the asterisk sign, the final form

$$\frac{D\Psi}{Dt} = \frac{1}{ReSc}\nabla^2\Psi.$$
(3.31)

3.1.4   The "one-fluid" formulation

The "one-fluid" formulation seeks to write the momentum equation without appealing to jump conditions at the interface. In this case, the fluids in the different phases apart are treated, in reality, as one sole fluid whose material properties vary abruptly across the interface. Forthwith, the insertion of singular terms into the formulation is required in order to account for the forces acting upon the interface. As declared in [?], this procedure brings up the feasibility of solutions that include generalized functions, such as δ-functions or step functions.

In this thesis, the Heaviside function $H(\mathbf{x})$ plays the role to identify the different fluid regions as well as the interface, i.e. the marker function. As pointed out by [?], it turns out that

$$H(\mathbf{x}) = \int_{A_I} \delta(x - x_I)\delta(y - y_I)\mathbf{n}\, dA_I, \quad \forall \mathbf{x} = (x, y).$$
(3.32)

Figure 20 is a sketch of Heaviside function's behaviour for two-dimensional domains. More-

over, it holds that

$$\nabla H = -\int_{A_I} \delta(x - x_I)\delta(y - y_I)\mathbf{n_I}\, dA_I = -\delta(\eta)\mathbf{n}, \tag{3.33}$$

where η is the coordinate normal to the interface in a local coordinate system aligned with the interface.

By defining the function δ_ζ, which is concentrated on the interface ζ in the same way as the Dirac δ-function is concentrated on a point, the following relation holds:

$$\delta_\zeta(\mathbf{x}_I) = \delta(\eta), \quad \mathbf{x}_I \in \zeta. \tag{3.34}$$

However, the function $\delta_\zeta(\mathbf{x}_I)$ has the property of converting volume integrals into surface integrals so that, for an arbitrary function f,

$$\int_V \delta_\zeta(\mathbf{x}_I) f(\mathbf{x}_I)\, dV = \int_\zeta f(\mathbf{x})\, dA_I. \tag{3.35}$$

Due to Equation (3.33), the gradient of the Heaviside function relates to the Dirac δ-function as

$$\nabla H = -\delta_\zeta \mathbf{n} = -\delta \mathbf{n}. \tag{3.36}$$
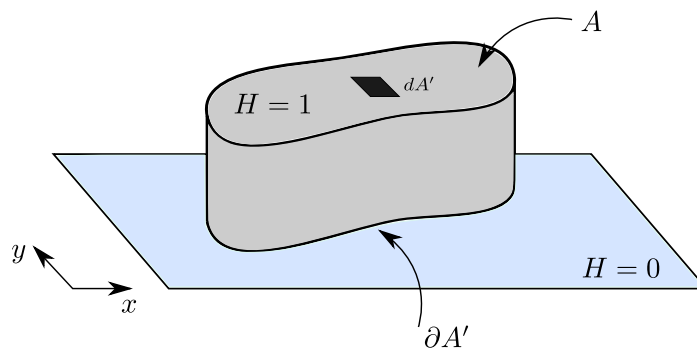
Figure 20: Representative behaviour of the Heaviside function over a two-dimensional surface. Adapted version from [?], p. 35.

Given these considerations, the surface force from Equation (2.22) is added to the

integral form through

$$\mathbf{f}_\zeta \delta_\zeta = \sigma \kappa \mathbf{n} \delta_\zeta, \tag{3.37}$$

whereby, the form

$$\mathbf{f} = \sigma \kappa \nabla H \tag{3.38}$$

gathering the effects of a sharp interface immersed in a arbitrary volume leads to

$$\rho \left(\frac{\partial \mathbf{v}}{\partial t} + (\mathbf{v} - \hat{\mathbf{v}}) \cdot \nabla \mathbf{v} \right) = -\nabla p + \nabla \cdot \left[\mu \left(\nabla \mathbf{v} + \nabla \mathbf{v}^T \right) \right] + \rho \mathbf{g} + \mathbf{f}. \tag{3.39}$$

In view of the CSF model introduced by Brackbill *et al.* [?], the additional surface force term appended to Equation (3.21) is distributed throughout the volume as a body force.

Additionally, following the standard steps to establish dimensionless quantities (cf. [?]), Equation (3.39) carried to a normalized and dimensionless domain renders

$$\rho^* \left(\frac{\partial \mathbf{v}^*}{\partial t} + (\mathbf{v}^* - \hat{\mathbf{v}}^*) \cdot \nabla^* \mathbf{v}^* \right) = -\nabla p^* + \frac{1}{Re} \nabla^* \cdot \left[\mu^* \left(\nabla^* \mathbf{v}^* + \nabla^* \mathbf{v}^{*T} \right) \right] + \frac{1}{Fr^2} \rho^* \mathbf{g}^* + \frac{1}{We} \mathbf{f}^*, \tag{3.40}$$

with the dimensionless groups

$$Re = \frac{U_{ref} L_{ref}}{\nu_{ref}}, \qquad Fr = \frac{U_{ref}}{\sqrt{g_{ref} L_{ref}}}, \qquad We = \frac{\rho_{ref} L_{ref} U_{ref}^2}{\sigma_{ref}}. \tag{3.41}$$

The latter variables are measures of reference, whereas the asterisk sign identify the dimensionless quantities that, without losing the generality, can, henceforth, be dropped out from the equation when referred.

Recalling that the divergence constraint in Equation (3.7) takes the dimensionless form

$$\nabla^* \mathbf{v}^* = 0, \tag{3.42}$$

after dropping out the asterisk, Equations (3.40) and (3.42) form the set of dimensionless governing equations to be solved for given initial and boundary conditions that set up a well-posed problem. In a reduced form, the set of partial differential equations which we stick

to is given by

$$B_1(\mathbf{v}, p, \mathbf{f}; \hat{\mathbf{v}}, \rho, \mu, \mathbf{g}) := \rho \frac{\hat{D}\mathbf{v}}{Dt} + \nabla p - \frac{1}{Re} \nabla \cdot \left[\mu \left(\nabla \mathbf{v} + \nabla \mathbf{v}^T \right) \right] - \frac{1}{Fr^2} \rho \mathbf{g} - \frac{1}{We} \mathbf{f} = \mathbf{0} \qquad (3.43a)$$

$$B_2(\mathbf{v}) := \nabla \cdot \mathbf{v} = 0, \qquad (3.43b)$$

$$B_3(\Psi) := \frac{D\Psi}{Dt} - \frac{1}{ReSc} \nabla^2 \Psi = 0, \qquad (3.43c)$$

with

$$\frac{\hat{D}\mathbf{v}}{Dt} = \left(\frac{\partial \mathbf{v}}{\partial t} + (\mathbf{v} - \hat{\mathbf{v}}) \cdot \nabla \mathbf{v} \right), \qquad (3.44)$$

so as to compact posterior algebrisms.

3.2 **Applied methods**

3.2.1 Projection method

Projection methods for incompressible flows have been applied since the late 1960's, when pioneer treatises grounded on time splitting techniques appeared [?], [?]. When these methods are applied to the Navier-Stokes equations, their gist unveils the interpretation of the equations as projections that lie on the Helmholtz-Hodge decomposition [?] (also known as Ladyzenhskaya theorem [?]), which is stated by the following theorem:

Theorem 3.2.1 (Helmholtz-Hodge decomposition) *A given vector field* **w** *is uniquely decomposed in a bounded domain* Ω *with smooth boundary* $\partial\Omega$ *as*

$$\mathbf{w} = \mathbf{v} + \nabla\phi, \qquad (3.45)$$

where ϕ *is a scalar field and* **v** *a vector field such that* $\nabla \cdot \mathbf{v} = 0$ *and* $\mathbf{v} \cdot \mathbf{n} = 0$, *i.e., for any vector* **n** *normal to* $\partial\Omega$, **v** *is parallel to* $\partial\Omega$.

Through this decomposition, velocity and pressure are uncoupled and elliptic equations are solved at each discrete time step. A organized review of projection methods given by Guermond *et al.* [?] separates them into three major classes: pressure-correction methods, velocity-correction methods, and the consistent splitting methods. In this thesis, in evocation to the third ensemble, a canonical splitting method based on exact LU factorization in two

blocks coined by Lee *et al.* [**?**] as of "type D" is used to tackle the coupling. Before exposing this particular choice, a few words about generalities of the projection method will be imparted next underpinned by Gresho and Sani's description (cf. [**?**], Section 3.16.6).

Awhile, we will write the incompressible Navier-Stokes equations in the traditional pressure-velocity version for single-phase flows as

$$\frac{\partial \mathbf{v}}{\partial t} + \nabla p = \mathbf{d} \tag{3.46}$$

$$\mathbf{d} \equiv \nu \nabla^2 \mathbf{v} + \mathbf{g} - \mathbf{v} \cdot \nabla \mathbf{v}. \tag{3.47}$$

Then, from the incompressibility constraint, one verifies that

$$\nabla \cdot \mathbf{v} \Rightarrow \nabla^2 p = \nabla \cdot \mathbf{d}. \tag{3.48}$$

Such Poisson-like equation implies

$$p = (\nabla^2)^{-1} \nabla \cdot \mathbf{d} \tag{3.49}$$

$$\nabla p = \nabla (\nabla^2)^{-1} \nabla \cdot \mathbf{d}, \tag{3.50}$$

which, in turn, renders Equation (3.46) into

$$\frac{\partial \mathbf{v}}{\partial t} = \mathbf{d} - \nabla p \tag{3.51}$$

$$= \mathbf{d} - \nabla (\nabla^2)^{-1} \nabla \cdot \mathbf{d}, \tag{3.52}$$

$$= \left[\mathbf{I} - \nabla (\nabla^2)^{-1} \nabla \cdot \right] \mathbf{d}, \tag{3.53}$$

$$\tag{3.54}$$

Now, two orthogonal projection operators leaping out from the latter equation can be identified, viz.

$$\mathsf{P} \equiv \mathbf{I} - \nabla (\nabla^2)^{-1} \nabla \cdot \tag{3.55}$$

$$\mathsf{Q} \equiv \mathbf{I} - \mathsf{P}, \tag{3.56}$$

$$\tag{3.57}$$

so that the projection-like form of the primary Navier-Stokes equations turns into

$$\frac{\partial \mathbf{v}}{\partial t} = \mathsf{P}\mathbf{d}(\mathbf{v}) \tag{3.58}$$

$$= \mathbf{d}(\mathbf{v}) - \nabla p \tag{3.59}$$

$$= \mathbf{d}(\mathbf{v}) - \mathsf{Q}\mathbf{d}(\mathbf{v}) \tag{3.60}$$

with Equations (3.58) and (3.59) delivering the interpretation that the operator P removes the gradient part of $\mathbf{d}$ to reveal its divergence-free part - the acceleration. Insofar that one shows the validity of

$$\nabla \cdot \mathsf{P} = 0 \tag{3.61}$$

$$\nabla \times \mathsf{Q} = 0, \tag{3.62}$$

the complete argument for the projection is sustained by the orthogonal decomposition

$$\mathbf{d} = \mathsf{P}\mathbf{d} + \mathsf{Q}\mathbf{d}, \tag{3.63}$$

i.e, while P projects $\mathbf{d}$ onto the null space of divergent and $\mathsf{P}\mathbf{d}$ is its divergence-free component, Q projects $\mathbf{d}$ onto the null space of curl and $\mathsf{Q}\mathbf{d}$ is its curl-free component.

To summarize, the recipe to obtain the solution $\mathbf{v}$ is stated as follows: guess ∇p; subtract it from $\mathbf{f}(\mathbf{v})$; integrate the result for some length of time coherent to the former guess, and project the final result to the divergence-free subspace. If the guess is perfect, then the divergence-free solution is readily attained; otherwise, a spurious divergence is obtained. In other words, given an incompressible velocity field at an initial time, say $t = 0$, that satisfies the boundary conditions imposed, the following steps should be performed:

i) Guess $\nabla p(\mathbf{x}, t)$ for $t \geq 0$;

ii) Solve the momentum equations alone, with $\nabla p(\mathbf{x}, t)$ acting as another given body force up to a "projection time" $t = t_m$ at which an appropriate norm of $\nabla \cdot \mathbf{v}^{\#}(\mathbf{x}, t_m)$ reaches some acceptable maximum value, where $\mathbf{v}^{\#}(\mathbf{x}, t_m)$ is an intermediary velocity not satisfying the divergence-free constraint;

iii) Project $\mathbf{v}^{\#}(\mathbf{x}, t_m)$ onto the nearest divergence-free subspace to obtain $\mathbf{v}(\mathbf{x}, t_m) = \mathsf{P}\mathbf{v}^{\#}(\mathbf{x}, t_m)$ and retain $\mathbf{v}(\mathbf{x}, t_m)$ as the Navier-Stokes velocity, thus finishing one projection cycle.

iv) Restart from the first step.

Because of the uncertainty and fallibility of the guesses, such projection-based methods generally have a considerable degree of sofistication to retrieve the divergence-free solution for the equations. However, several of the proposed techniques not always admit a favourable computational implementation, thus falling back into numerical struggles to deal with the paramount problem of the coupling.

3.2.2 Semi-Lagrangian method

The Semi-Lagrangian method gained renown with applications turned to meteorological predictions and climatic phenomena, as seen in [?] and [?]. Having an intrinsic property of allowing numerical simulations managed by long time steps, its benefits to public safety, environment, and economy can be readily recognized. Accurate climatic predictions, for instance, may support urgent decision makings in prospective scenarios of natural disasters, thus helping to mitigate eventual damages, restrain severe losses, and secure an entire population. Historical background and a general review about the method's development in the ambit of the Meteorology is found in [?] and [?].

Aside from its original field, the use of the SL method in other scientific areas had already been advocated [?], so that different names were coined to express it, such as *Method of Characteristics* and *Method Eulerian-Lagrangian* [?]. Concerning its infusion into the finite element's ground, pristine contributions blossomed from [?], at which a numerical algorithm to solve the advection-diffusion equation was intended.

The basis of the SL method focuses on a *backward-in-time* integration whereby the fluid particle trajectories are tracked with the time and can be explained by opting for an advection problem defined on the set $\Omega \times \tau$, with $\tau = \bigcup_{n=0}^{L-1} [nt, (n+1)t]$ being the union of time intervals. If $\mathbf{x} \in \Omega$ is a spatial position through which the particle χ travels and $\{X(\tau)\}_{nt \leq \tau \leq (n+1)t}$ is the solution of the differential equation

$$\frac{dX(\tau)}{d\tau} = \mathbf{v}[X(\tau), \tau], \tag{3.64}$$

then $X(\tau)$ is the trajectory traced by the particle χ within the time range $[nt, (n+1)t]$ -

elsewhere t^n, t^{n+1} - and also a characteristic of the compact equation

$$\frac{\partial \boldsymbol{\Phi}}{\partial \tau} + \mathbf{v} \cdot \nabla \boldsymbol{\Phi} = \boldsymbol{F}, \tag{3.65}$$

for $\boldsymbol{\Phi} = (\Phi_1, \Phi_2, \dots, \Phi_N)$, the vector of N fluid variables, and $\boldsymbol{F} = (F_1(\boldsymbol{\Phi}), F_2(\boldsymbol{\Phi}), \dots, F_N(\boldsymbol{\Phi}))$, the vector of N source terms.

With $\mathbf{x}$ and t being parameters for the trajectory, we write $\boldsymbol{X}(\tau) = \boldsymbol{X}(\mathbf{x}, t; \tau)$. By defining $\mathbf{x}_\# = \boldsymbol{X}(\mathbf{x}, nt; \tau)$ as the position occupied by the particle at the instant $\tau = nt$ and $\mathbf{x}_a = \boldsymbol{X}(\mathbf{x}, (n+1)t; \tau)$ as the position occupied by the particle at the instant $\tau = (n+1)t$, the goal of the SL method is achieved when the point $\mathbf{x}_d$, an approximation to the true departure point $\mathbf{x}_\#$, is found after integrating Equation (3.65) backward-in-time. Precisely, the determination of $\mathbf{x}_d$ obeys a relation such that

$$(\mathbf{x}_d, nt; \tau) \approx (\mathbf{x}_\#, nt; \tau) = (\mathbf{x}_a, (n+1)t; \tau) - \int_{nt}^{(n+1)t} \mathbf{v}(\boldsymbol{X}(\mathbf{x}, \tau)) d\tau, \tag{3.66}$$

i.e., the observed particle reposes exactly on the site $\mathbf{x}_a$ at the time $\tau = (n+1)t$. Furthermore, it holds (e.g., see Eq. 4 of [?])

$$\boldsymbol{\Phi}(\mathbf{x}_a, (n+1)t; \tau) = \boldsymbol{\Phi}(\mathbf{x}_d, nt; \tau) + \int_X (d\mathbf{x} - \mathbf{v}d\tau) \cdot \nabla \boldsymbol{\Phi} + \int_X \boldsymbol{F} d\tau. \tag{3.67}$$

Over the years, the numerical development of the SL method spreaded variably. The first approximations for the trajectories, however, were based on simple straight lines. Thereafter, high-order time-splitting schemes arose [?] [?]. In this thesis, the material derivative in the form of Equation (3.65) is approximated by

$$\frac{D\boldsymbol{\Phi}}{D\tau} = \frac{\partial \boldsymbol{\Phi}}{\partial \tau} + \mathbf{v} \cdot \nabla \boldsymbol{\Phi} \approx \frac{\boldsymbol{\Phi}(\mathbf{x}_a, (n+1)t; \tau) - \boldsymbol{\Phi}(\mathbf{x}_d, nt; \tau)}{\Delta t}, \tag{3.68}$$

where Δt is the time step. In such format, the gradient $\nabla \boldsymbol{\Phi}$ is suppressed on the computations, meaning that the temporal rate of change plus the convective rate of change occur instantaneously in a combined effect. In turn, $\mathbf{x}_d$ is obtained through

$$(\mathbf{x}_d; \tau) = (\mathbf{x}_a; \tau) - \boldsymbol{\alpha}.$$

Here, $\boldsymbol{\alpha}$ depends on a known velocity at a previous time step which is computed through the

linear approximation

$$\boldsymbol{\alpha} = \Delta\tau\mathbf{c}(\mathbf{x}_a, nt; \tau) = \Delta\tau(\mathbf{v} - \hat{\mathbf{v}})(\mathbf{x}_a, nt; \tau). \tag{3.69}$$

Generally, such approximations result in departure points that do not match any mesh point. Therefore, $\boldsymbol{\Phi}(\mathbf{x}_d, nt; \tau)$ must be calculated by means of some interpolation. For these reasons, trajectory integration and interpolation are the constitutive elements of any SL scheme [**?**]. With the increasing development of high-order methods, theoretical error analyses as well as optimization factor reports related to SL methods were published, of which a known expression for the order of the advection average error of the method was derived, namely,

$$\mathscr{O}\left(\Delta t^r + \frac{\Delta\mathbf{x}^{p+1}}{\Delta t}\right),$$

where r and p here stand for the order of trajectory integration and of interpolation, respectively [**?**].

Although this study is based on an ALE context, the SL methodology might seem abstruse due to its peculiarities. On the one hand, the location of the departure point through the backwards calculation Equation (3.69) uses the relative velocity $\mathbf{c}$ for the advective regression so as to gather both the Lagrangian and Eulerian effects as desired. On the other hand, the velocity interpolated near the foot of the trajectory carries a purely Lagrangian contribution that feeds back the iterative process of the computational code within each time step only. In other words, one observes the existence of an abstract mesh which distorts at each discrete time interval. Figure 21, adapted from [**?**] enlightens these events inside a spatio-temporal context over a two-dimensional triangular mesh that disregards, for clarity, the mesh movement caused by interference of the ALE dynamics. $(\mathscr{T}_{\mathbf{X}}^h, (n+1)t)$ and $(\mathscr{T}_{\mathbf{X}}^h, nt)$ represent two "slices" of the same triangulation at the two time instants analyzed.

The Eulerian mesh is drawn in thick borders, which keeps fixed along the time. The Lagrangian mesh, on the other hand, is formed when the isolated points that spread over the Eulerian mesh are joint by abstract edges, as seen through the gray-filled portion drawn on the same plane where the Eulerian mesh lies on. Additionally, the long-dashed lines starting from the points over the Lagrangian mesh at the instant $\tau = nt$ and arriving at the points of the Eulerian mesh at the time $\tau = (n+1)t$ represent the particle trajectories. Among them, the trajectory $\mathbf{X}(\tau)$, leaving $\mathbf{x}_\#$ and arriving at $\mathbf{x}_a$ is highlighted. The isolated
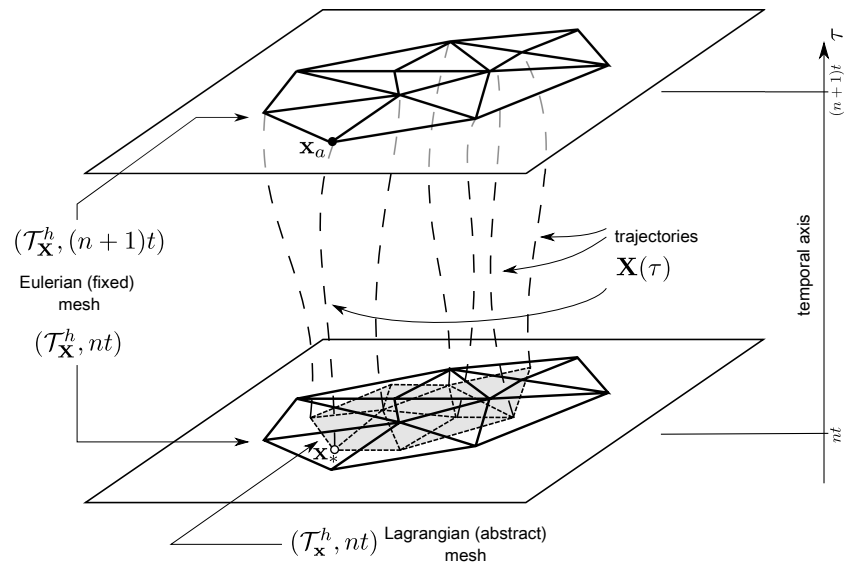
Figure 21: SL method in a spatio-temporal context over a two-dimensional triangular finite element mesh displaying the Lagrangian "abstract" mesh.

points before mentioned are, therefore, the departure points (or "feets", alternatively) of the characteristic curves already mentioned. This explanation, in turn, just reinforces the concept of an Eulerian-Lagrangian approach, which combines both descriptions.

4 FINITE ELEMENT PROCEDURES IN TWO-PHASE FLOWS

The purpose of this chapter is to discourse about theoretical and computational aspects of the FEM with special attention to the gas-liquid two-phase flow dynamics and to concepts related to this thesis. A few considerations on the historical background of the method, however, give occasion to divert out from the Fluid Dynamics momentarily for a better clarification. This is, in turn, the object of the opening section, which has by progression a series of theoretical topics studied in developing the FEM. The part of the text corresponding to more applied contents comes soon after in the sequel.

4.1 Historiography and theory of the classical FEM

From the birth of the FEM as numerical method to solve partial differential equations, the Engineering follows its remarkable uprise until the present time by recognizing it as a robust tool capable to branch in many different facets. In reality, the term FEM was coined by Prof. Ray W. Clough in the 1960's after a premature version before known as *Direct Stiffness Method*, although exist arguments favourable to the FEM's creation dating back the Leibniz's ages between the XVII and XVIII centuries, when the variational methods were being developed. From these early times, the tied union with the Mathematics elevated the scientific community to sovereign levels of rigour and formalism while clothing the FEM in a solid armour. On the other hand, this process caused a bifurcation in the sense of how to interpret the FEM, dissociating the mathematical current from the physical one. While the former was used to see the FEM under a structural/mechanical basis, the latter accustomed the eyes to see the FEM as a functional/variational problem, both of which getting the same results. The analogy of dividing a domain in smaller pieces called "elements", for instance, is not as complete as the mathematical definition, which requires further attention.

In 1943, Courant presented the so-called *Courant element*, which is the fundamental element formed by a triangle equipped with linear piecewise functions. Afterwards, many others arose as byproducts of compositions, such as the family of *Hermite elements*, *Argyris elements* and *Crouzeix-Raviart elements*, all of them derived from a triangular geometry, but differing by the set of degrees of freedom. In this case, they consider nodal evaluations of either only functions, or functions and directional derivatives, or still functions and higher order derivatives. Figure 22, adapted from [**?**], illustrates a couple of elements. The arrows in

the Argyris element symbolize the normal derivative evaluated at the midpoints of the edges. Similar ideas extend to other dimensions and geometries, producing new elements.
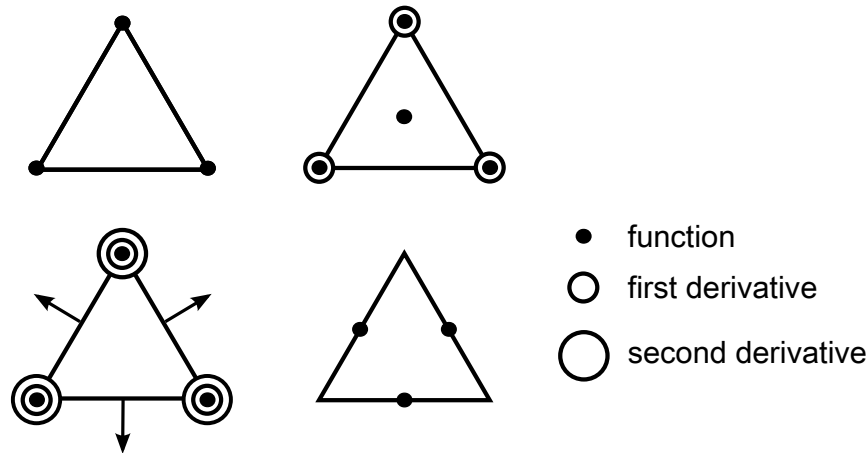
Figure 22: Different two-dimensional compositions: the Courant element, the Hermite element, the quintic Argyris triangle and the nonconforming linear Crouzeix-Raviart triangle (arranged from left to right/top to bottom).

Although the mathematics of FEM flowed independently also with considerable advancements in a functional scope concerning minimization problems and variational forms as previously authored by Ritz and Galerkin in 1910's decade, problems of the structural mechanics boosted the FE research after the period of the II World War, whose interests turned to aircraft engineering, and later, with contributions of renowned corporations, such as IBM, NASA and Boeing. This time was essential to promote the known literature written by Zienkiewicz [?] as well as the ascension of the sovietic influence worldwide with Friedrichs, Petrov and Galerkin's legacy.

In the 1970's, several mathematical books about FEM appeared, including the Strang & Fix's classical book [?]. From this moment on, the most classical FEM acquired variants, such as: the *Generalized FEM (GFEM)* [?], [?], which uses not only polynomial spaces as base functions; the *hp-FEM*, which combines adaptive refinement h with polynomial orders p [?]; and the *Extended FEM (XFEM)*, which embeds discontinuous functions to enrich spaces of GFEM [?]. In addition to such an variants, the formulations currently known as *SUPG (Streamline-Upwind Petrov-Galerkin)* [?], *GLS (Galerkin-Least Squares)* [?] and *PSPG (Pressure-Stabilized Petrov-Galerkin)* play a fundamental role in the development of stabilized methods in FE history for both compressible and incompressible dynamics. The so-called *PFEM (Particle-Finite Element Method)* [?] and *NEFEM (NURBS-enhanced finite element method)* [?] also correspond to different branches in the series of FE methods hitherto.

More recently, emphasis has been given to fluid-structure interaction (FSI) computations, for which several FE-related methods were devised. They include multiscale space-time techniques [?], [?], isogeometric analysis and NURBS (Non-Uniform Rational B-Splines) [?] and ALE methods [?], [?], such as one discusses in this thesis, which also is widely known in FSI problems. For an overview of stabilized methods, see [?]; for future trends and current challenges in FSI modelling, see [?].

A vast list of ancient and modern literatute of FEM could not be described here. For brevity, however, the following authors are enough erudite recommendations to know about the multivalency of the FEM, namely, Ciarlet [?], Zienkiewicz & Taylor [?], Reddy [?], Hugues [?], Johnson [?], Wait & Mitchell [?], Girault & Raviart [?], Ern & Guermond [?], [?], among others. This modest bibliography brings up the FEM both theoretically, numerically and computationally. Historical notes about the FEM as summarized here can be found in [?].

Basically, the FEM is directly linked to the search for a function u that minimizes a given expression of energy. Assuming that the problem to be solved admits a variational formulation which, for an arbitrary differential operator L and a given function f, holds an expression like

$$\mathsf{L}u = f, \tag{4.1}$$

for certain initial and boundary conditions, the method can be summarized in the following steps:

i) Find the variational form of the problem;

ii) Construct a basis of piecewise polynomial trial functions;

iii) Assemble and solve the matrix discrete system;

iv) Estimate the accuracy of the approximation.

To determine the variational or weak form of a finite element problem according to the classical approach, weight functions are used as well as Ritz-Galerkin approximations. Thus, by adjourning details until posterior sections, the weak form of Equation (4.1) reveals in the form

$$(\mathsf{L}u, w) = (f, w), \tag{4.2}$$

for a given weight function w and operations of inner products $(\cdot,\cdot)$ well defined. Thenceforth, function spaces are created to set forth approximations $u \approx u_h$, $f \approx f_h$, so that Equation (4.2) is written as

$$(\mathsf{L}u_h, w_h) = (f_h, w_h). \tag{4.3}$$

Such discretized bilinear forms, in turn, are conducted to a n-dimensional matrix equation in the form

$$\mathbf{L}\mathbf{u}_h = \mathbf{b}, \tag{4.4}$$

of which $\mathbf{u}_h = \mathbf{L}^{-1}\mathbf{b} \in \mathbb{R}^m$ is the solution. Since $\mathbf{u}$ would be, indeed, the vector storing the exact values of the solution evaluated pointwise on the discrete domain, the accuracy of the final result must be estimated through an error expression as

$$\mathbf{e} = ||\mathbf{u} - \mathbf{u}_h||, \tag{4.5}$$

where $\mathbf{e}$ can have different norm-based definitions.

4.2 FEM for incompressible two-phase flows

The list of procedures discussed so far presented the fundamental FEM techniques usually handled in Engineering as a whole. It matters now focusing on the FEM contribution to the field of incompressible two-phase flows, in preparation to the contents to be discussed in the rest of this chapter. Meanwhile, it is instructive to recall the classical definition of a finite element (e.g., see [**?**], p. 19, or [**?**], p. 78).

Definition 4.2.1 (Finite element) *Let*

i) $T \subseteq R^m$ be a compact, connected, Lipschitz subset with nonempty interior (the element domain);

ii) $\mathscr{P}$ be a vector space of functions $\varphi : T \to \mathbb{R}^m$ for some positive integer m (typically $m <= 3$) (the shape functions);

iii) $\mathscr{Y} = \{\varsigma_1, \varsigma_2, \ldots, \varsigma_l\}$ is a basis for $\mathscr{P}'$, the dual set of $\mathscr{P}$ (the nodal variables).

Then, $(T, \mathscr{P}, \mathscr{Y})$ is called a **finite element**.

Despite of Definition 4.2.1, in Engineering it is common practice use T only as the finite element itself.

4.2.1 Explicit representation of interfaces

In Section 2.4, some definitions were established to organize the construction of a two-phase discretized domain with independent mesh subsets, i.e., the *surface mesh* and the *volume mesh*. Although this separation is well clarified, the following lines will be dedicated to the discrete representation of the interface, by considering the ALE methodology quoted throughout the text.

Following similar ideas exposed by [?], we seek to characterize the interface by a explicit representation. For this purpose, Figure 23 and Figure 24 will serve as a guide. If **n** is a normal unit vector placed at the interface pointing toward the liquid phase, we consider that the arbitrary motion of a curve is oriented as this vector, having a positive displacement if the local interface velocity points toward the same direction as **n** and negative otherwise.
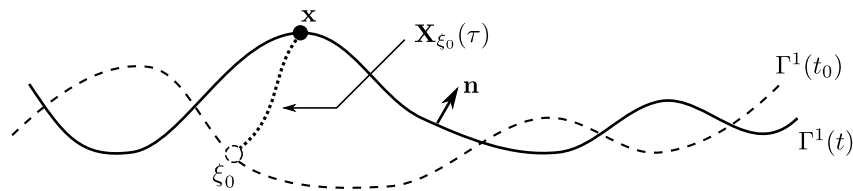
Figure 23: Two-time representation of a continuous interface Γ^1. Dashed: time t_0; thick: time t; dotted: trajectory.
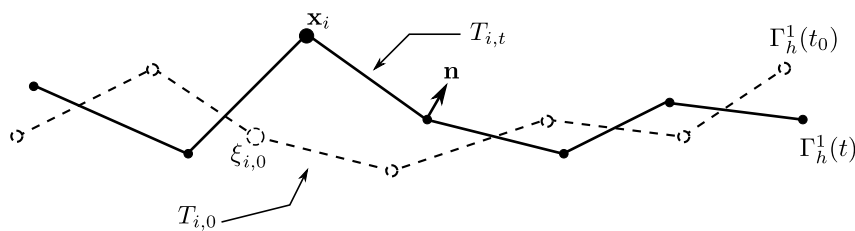
Figure 24: Two-time representation of a piecewise linear interface Γ_h^1. Dashed: time t_0; thick: time t; dotted: trajectory.

Then, let $\Gamma^1(t_0), \Gamma_h^1(t_0)$ and $\Gamma^1(t), \Gamma_h^1(t)$ be the continuous and discrete interfaces at two time instants $t_0, t, t > t_0$. As already defined in Section 2.4, $\Gamma_{h_1}^1$ is a tessellation of the interface which, in this simpler example, is made up by linear elements. That said, the *interface tracking*

methodology relies on the validity of the relation

$$\Gamma(t) \ni \mathbf{x} = \xi_0 + \int_{t_0}^{t} \hat{\mathbf{v}}(\mathbf{X}_{\xi_0}(\tau), \tau) \, d\tau, \quad \xi_0 \in \Gamma(t_0), \quad t \geq t_0, \tag{4.6}$$

where $\mathbf{x}$ is the position at t reached by a particle that travels with the time τ following the trajectory $\mathbf{X}_{\xi_0}(\tau)$ after the interface is advected with velocity $\hat{\mathbf{v}}$. When contrasting the continuous and discrete versions of the illustrations, ξ_0 ($\xi_{i,0}$) means a point of the continuous (discrete) interface at the time t_0, while $\mathbf{x}$ ($\mathbf{x}_i$) so is at the time t. Equation (4.6), hence, exhibits a Lagrangian point of view widely used in numerical methods based on interface tracking. Thus, in fact, due to the mesh movement, it turns out that

$$\Gamma^1_{h_1}(\tau) := \{T(\tau) \in \mathcal{T}_h(\tau); \ H(\mathbf{x}_i) = 0.5\}, \quad i = 1, 2, \ldots, \iota, \quad \tau \in [t_0, t] \tag{4.7}$$

for ι mesh nodes. Moreover, this condition is respected everywhere for an interface due to the mesh construction, thus ensuring the perdurable status of thin thickness. In Figure 24, for example, is highlighted the movement of the element T_i, which has $\mathbf{x}_i$ as one of its nodes.

4.2.2 Adaptive refinement: thresholds and transfinite interpolation

Given the need of better accuracy in the neighbourhood of interfaces as well as in their own representation, some techniques of adaptive refinement are applied here and depicted in Figure 25. The left drawing considers thresholds from which the transition of
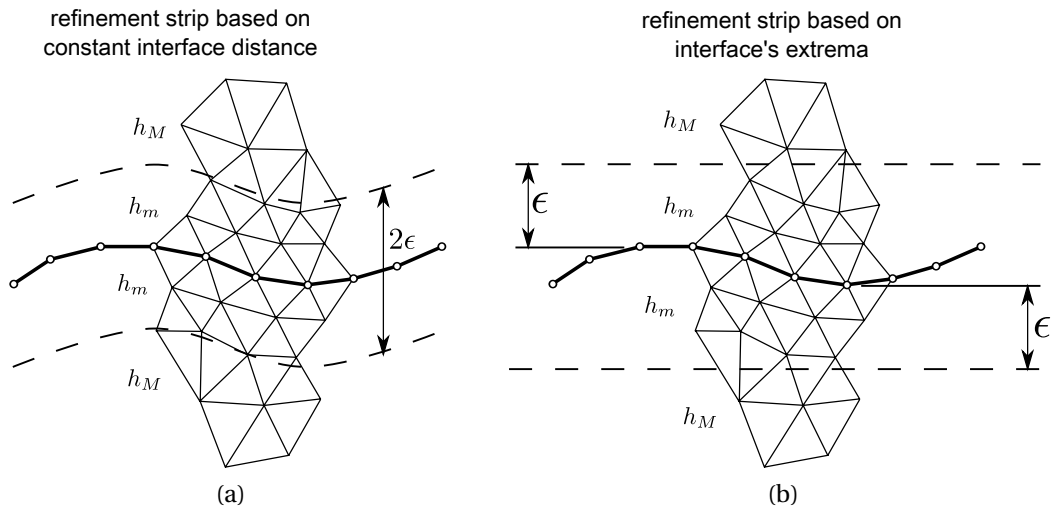
Figure 25: Adaptive refinement strategies applied at interfaces and neighborhoods: (a) criterion based on constant distance; (b) criterion based on distance from the extrema points.

characteristic size of the elements belonging to $\mathcal{T}_h^\Omega$ takes place. They are determined by fixing an user-defined distance ϵ that establishes the neighborhood $N_\epsilon[\Gamma_h]$, which encircles a certain topological region of space (e.g. a strip in 2D; a tube, or sphere, in 3D). On the other hand, the right drawing uses the extrema points of a wambled interface to establish thresholds further above of the maximum absolute or further below of the minimum absolute. In a generalized way, we can write

$$\overline{h}_T = \left\{ \begin{array}{ll} h_m, & \text{if } T \in N_\epsilon[\Gamma_h] \\ h_M, & \text{if } T \notin N_\epsilon[\Gamma_h] \end{array} \right. ,$$

where $\overline{h}$ is a mean element size. That is to say, $h_m < h_M$.

In addition to thresholds, transfinite meshing can be applied for the interfaces through a denser distribution of nodes as depicted in the drawing at right. However, differently than the previous strategy, which can be recalled during the simulation and parametrized over again, this method is used in the pre-processing stage simultaneously with the mesh construction. Together with the first technique, such an approach provide a wide range of adaptive refinement for the control parameter h relative to the interface mesh.

4.3 Variational formulation of the governing equations

4.3.1 Primitive variables

Pioneer researches introducing a variational (or weak) form of the incompressible Navier-Stokes arose some decades ago for the single-phase universe [**?**]. On the other hand, extensions to two-phase flows based on FE are more juvenile not only by the epoch, but also because of variants arising from the different ways wherewith methods deal with interfaces and curvatures (see, e.g., [**?**], [**?**], [**?**], [**?**]). The approach used here follows the same derivation for the single-phase dynamics exposed in [**?**] plus the two-phase increments introduced in [**?**]. Therefore, most of the algebraic details will be omitted.

A recipe to obtain the weak formulation sought is given in [**?**] as regards as the *Integrated Method*, which, sealed with the approach of weighted residual, is summarized as follows: to multiply the governing equations by arbitrary test functions; to integrate them over the domain; to apply partial integration, if necessary, and finally to impose the boundary conditions. Above all, let us define some necessary functional settings on $\Omega = \Omega^1 \cup \Omega^2$.

The Sobolev space $\mathcal{H}^1$ in Ω is the set

$$\mathcal{H}^1(\Omega) := \left\{ \mathbf{u} \in \mathcal{L}^2(\Omega) \, ; \, \frac{\partial \mathbf{u}}{\partial x_i} \in \mathcal{L}^2(\Omega), i = 1, 2, \ldots, m \right\}.$$

For reasons of application, a simpler writing was preferred instead of the multi-index notation. Above, $\mathcal{L}^2(\Omega)$ is the set of the square-integrable functions in the sense of Lebesgue [?], defined by

$$\mathcal{L}^2(\Omega) := \left\{ \mathbf{u} := \Omega \to \mathbb{R}^m \, ; \, \left(\int_\Omega ||\mathbf{u}||^2 \, d\Omega \right)^{1/2} < \infty \right\}.$$

The determination of functions of approximation over the finite element is sensitive to the construction of a functional basis linearly independent that can generate a finite dimensional space from an infinite dimensional space called the *trial functions* space. Once the incompressible Navier-Stokes equations have a mixed nature in the sense of coupling velocity and pressure, spaces of trial functions should be chosen conveniently. Then, we include the Sobolev spaces given by

$$\mathcal{S} := \left\{ \mathbf{u} \in \mathcal{H}^1(\Omega) \, ; \, \mathbf{u} = \mathbf{u}_D \ \text{in} \ \Gamma_{D,\mathbf{u}} \subseteq \Gamma_D \right\}.$$

$$\mathcal{Q} := \left\{ q \in \mathcal{L}^2(\Omega) \, ; \, q = q_D \ \text{in} \ \Gamma_{D,q} \subseteq \Gamma_D \right\}.$$

Additionally, the *weight functions* space is defined as:

$$\mathcal{V} := \left\{ \mathbf{w} \in [\mathcal{H}^1(\Omega)]^m \, ; \, \mathbf{w} = \mathbf{0} \ \text{in} \ \Gamma_D \right\},$$

where $[\mathcal{H}^1(\Omega)]^m = \mathcal{H}^1(\Omega) \times \ldots \times \mathcal{H}^1(\Omega)$ is the $m-$times cartesian product of $\mathcal{H}^1$, $\mathbf{u}_D$ is the value of the Dirichlet condition over the boundary Γ_D.

From $\mathcal{S}$, $\mathcal{Q}$, $\mathcal{V}$, the spaces $\mathcal{S}^h \subset \mathcal{S}$, $\mathcal{Q}^h \subset \mathcal{Q}$ and $\mathcal{V}^h \subset \mathcal{V}$ are extracted, both having finite dimension in the sense of a $h-$refinement related to the level of mesh discretization [?]. Thus,

$$\mathcal{S}^h := \{ \mathbf{u}^h \in \mathcal{H}^1(\Omega) \, ; \, \mathbf{u}^h = \mathbf{u}_D \ \text{in} \ \Gamma_{D,\mathbf{u}} \subseteq \Gamma_D \},$$

$$\mathcal{Q}^h := \{ q^h \in \mathcal{L}^2(\Omega) \, ; \, q^h = q_D \ \text{in} \ \Gamma_{D,q} \subseteq \Gamma_D \}$$

and

$$\mathcal{V}^h := \{\mathbf{w}^h = (w_1^h, w_2^h, \ldots, w_m^h) \in [\mathcal{H}^1(\Omega)]^m(\Omega)\,; \mathbf{w}^h = \mathbf{0} \text{ in } \Gamma_D\},$$

Being Γ Lipschitz, a general way of decomposing it reads as

$$\Gamma = \Gamma_D \cup \Gamma_N.$$

Γ_D is the *Dirichlet* boundary, or of *essential conditions*, wheras Γ_N is the *Neumann* boundary, or of *natural conditions*, i.e $\mathbf{u}$ can assume values such that

$$\mathbf{u}|_{\Gamma_D} = \mathbf{u}_D$$
$$\mathbf{u}|_{\Gamma_N} := \mathbf{n} \cdot \nabla \mathbf{u} = \mathbf{u}_N,$$

where $\mathbf{n}$ is a unit vector normal to Γ_N. It may be shown that the second condition is satisfied by the own weak formulation, whereby the metonym *natural* is suggested.

Now, by weighting the strong form given by Equations (3.43a) and (3.43b), we get

$$\int_\Omega \mathsf{B}_1(\mathbf{v}, p, \mathbf{f}; \hat{\mathbf{v}}, \rho, \mu, \mathbf{g}) \cdot \mathbf{w}\, d\Omega = \mathbf{0}, \quad \mathbf{w} \in \mathcal{V} \tag{4.8a}$$

$$\int_\Omega \mathsf{B}_2(\mathbf{v})\, q\, d\Omega = 0, \quad q \in \mathcal{Q}, \tag{4.8b}$$

which are expanded in the sum of integrals

$$\int_\Omega \rho \left(\frac{\partial \mathbf{v}}{\partial t} + (\mathbf{v} - \hat{\mathbf{v}}) \cdot \nabla \mathbf{v} \right) \cdot \mathbf{w}\, d\Omega + \int_\Omega \nabla p \cdot \mathbf{w}\, d\Omega$$

$$-\frac{1}{Re} \int_\Omega \nabla \cdot \left[\mu \left(\nabla \mathbf{v} + \nabla \mathbf{v}^T \right) \right] \cdot \mathbf{w}\, d\Omega - \frac{1}{Fr^2} \int_\Omega \rho \mathbf{g} \cdot \mathbf{w}\, d\Omega - \frac{1}{We} \int_\Omega \mathbf{f} \cdot \mathbf{w}\, d\Omega, = \mathbf{0} \tag{4.9a}$$

$$\int_\Omega (\nabla \cdot \mathbf{v})\, q\, d\Omega = 0. \tag{4.9b}$$

In turn, the parcels above can be written as bilinear forms defined by means of inner products

as

$$m_\rho\left(\rho;\frac{\hat{D}\mathbf{v}}{Dt},\mathbf{w}\right) := \int_\Omega \rho\frac{\hat{D}\mathbf{v}}{Dt}\cdot\mathbf{w}\,d\Omega, \tag{4.10a}$$

$$g(p,\nabla\cdot\mathbf{w}) := \int_\Omega p\nabla\cdot\mathbf{w}\,d\Omega, \tag{4.10b}$$

$$k(\mu;\nabla\mathbf{v},\nabla\mathbf{w}) := \int_\Omega \mu(\nabla\mathbf{v}+\nabla\mathbf{v}^T):\nabla\mathbf{w}^T\,d\Omega, \tag{4.10c}$$

$$m_\rho(\rho;\mathbf{g},\mathbf{w}) := \int_\Omega \rho\mathbf{g}\cdot\mathbf{w}\,d\Omega, \tag{4.10d}$$

$$m(\mathbf{f},\mathbf{w}) := \int_\Omega \mathbf{f}\cdot\mathbf{w}\,d\Omega, \tag{4.10e}$$

$$d(\nabla\cdot\mathbf{v},q) := \int_\Omega (\nabla\cdot\mathbf{v})q\,d\Omega. \tag{4.10f}$$

At this point, some comments should be weaved: firstly, the term $m_\rho\left(\rho;\frac{\hat{D}\mathbf{u}}{Dt},\mathbf{v}\right)$ relative to the advection is kept in a concentrated form for posterior use of a Semi-Lagrangian approximation for the material derivative; secondly, integrations by parts are implicitly embedded in these forms; lastly, the integrals related to Neumann boundaries vanish due to the natural condition.

Therewith, the weak form of Equations (3.43a) and (3.43b) turns into finding the solution of the system

$$m_\rho\left(\rho;\frac{\hat{D}\mathbf{v}}{Dt},\mathbf{w}\right) + g(p;\nabla\cdot\mathbf{w}) - \frac{1}{Re}k(\mu;\nabla\mathbf{v},\nabla\mathbf{w}) - m_\rho(\rho;\mathbf{g},\mathbf{w}) - \frac{1}{We}m(\mathbf{f},\mathbf{w}) = \mathbf{0} \tag{4.11a}$$

$$d(\nabla\cdot\mathbf{v},q) = 0. \tag{4.11b}$$

Nonetheless, the discrete version of Equations (4.11a) and (4.11b) needs to be invoked as

$$m_\rho\left(\rho;\frac{\hat{D}\mathbf{v}_h}{Dt},\mathbf{w}_h\right) + g(p_h;\nabla\cdot\mathbf{w}_h) - \frac{1}{Re}k(\mu;\nabla\mathbf{v}_h,\nabla\mathbf{w}_h)$$

$$-m_\rho(\rho;\mathbf{g}_h,\mathbf{w}_h) - \frac{1}{We}m(\mathbf{f}_h,\mathbf{w}_h) = \mathbf{0} \tag{4.12a}$$

$$d(\nabla\cdot\mathbf{v}_h,q_h) = 0. \tag{4.12b}$$

From [?], it is argued that the Galerkin method is the most useful regarding the computational feasibility. In this method, both the trial and weight functions are chosen to dwell in the same space. Furthermore, considering that Equations (4.11a) and (4.11b) are unsteady, a semidiscrete version should be used, i.e. the hypothesis is to assume that there are linear combinations of functions for which the coefficients of each shape function depend on time,

while the shape functions themselves vary only with the spatial coordinates. Thus, for a scalar function $u(\mathbf{x}, t) : (\Omega \times \tau) \to \mathbb{R}$ and a basis of shape functions $\{\varphi_i\}, i = 1, 2, \ldots, \iota$, the global Ritz-Galerkin approximation is given by

$$u(\mathbf{x}, t) \approx u_h(\mathbf{x}, t) := u^D + \sum_{i=1}^{\iota} a_i(t) \varphi_i(\mathbf{x}), \quad a_i(t) \in \mathbb{R}, \tag{4.13}$$

where $u^D = u_h^D \in \mathbb{R}$ is the value of an essential boundary condition imposed on the formulation. That is to say, if $u|_{\Gamma_D} = u^D \approx u_h^D$, then, it holds a relation such as

$$\mathscr{S}^h = \mathcal{V}^h \oplus \{\mathbf{u}_h^D\}, \quad \forall \mathbf{u}_h \in [\mathscr{H}^1(\Omega)]^m,$$

for a vector of functions $\mathbf{u}_h$ consistent with the dimension $m \leq 3$.

As aforementioned, the advective term is treated according to a Semi-Lagrangian approach [?] so that

$$\frac{\hat{D}\mathbf{v}_h}{Dt} \approx \frac{\mathbf{v}_h^{n+1} - \mathbf{v}_{h,d}^n}{\Delta t}. \tag{4.14}$$

Such a form stores the advection and ALE effects in a backward-in-time integration of the particle trajectories as explained in Subsection 3.2.2, which has $\mathbf{v}_{h,d}^n$ as the velocity of the departure point per trajectory. However, the search for the departure point should take into account the mesh movement introduced by the ALE formulation falling over the displacement vector $\boldsymbol{\alpha}$ (cf. Equation (3.66)) the need of store the contribution provided by the mesh velocity. Thus,

$$(\mathbf{x}_d; \tau) = (\mathbf{x}_a; \tau) - \mathbf{c}_h(\mathbf{x}_a)\Delta t, \quad \mathbf{x}_a \text{ of } T \in \mathscr{T}_h. \tag{4.15}$$

By introducing Equation (4.14) into Equation (4.12a) - safeguarded Equation (4.15) - and considering that Equation (4.13) is implicitly taken into account for both Equations (4.12a) and (4.12b), the semidiscrete version in space and time is given by

$$(\rho; \mathbf{v}_h^{n+1}, \mathbf{w}_h) + \frac{\Delta t}{Re}(\mu; \nabla \mathbf{v}_h^{n+1}, \nabla \mathbf{w}_h) + \Delta t(p_h^{n+1}, \nabla \cdot \mathbf{w}_h) =$$
$$= \Delta t \left[(\rho; \mathbf{v}_{h,d}^n, \mathbf{w}_h) + \frac{1}{Fr^2}(\rho; \mathbf{g}_h^n, \mathbf{w}_h) + \frac{1}{We}(\mathbf{f}_h^n, \mathbf{w}_h) \right] \tag{4.16a}$$

$$(\mathbf{v}_h^{n+1}, \nabla \cdot q_h) = 0 \tag{4.16b}$$

Since Equations (4.16a) and (4.16b) are bilinear forms already discretized, the introduction of a suitable finite element space and ensuing assembling mounting at element-level produces matrices such that, in the respective order, these equations render

$$\mathbf{M}_\rho \mathbf{v}^{n+1} + \frac{\Delta t}{Re} \mathbf{K} \mathbf{v}^{n+1} + \Delta t \mathbf{G} \mathbf{p}^{n+1} = \Delta t \left[\mathbf{M}_\rho \mathbf{v}_d^n + \frac{1}{Fr^2} \mathbf{M}_\rho \mathbf{g}^n + \frac{1}{We} \mathbf{M} \mathbf{f}^n \right] \tag{4.17a}$$

$$\mathbf{D} \mathbf{v}^{n+1} = \mathbf{0} \tag{4.17b}$$

Concisely, we can write $\mathbf{B} = \mathbf{M}_\rho + \dfrac{\Delta t}{Re} \mathbf{K}$ and arrange the equations to give

$$\begin{bmatrix} \mathbf{B} & \Delta t \mathbf{G} \\ \mathbf{D} & \mathbf{0} \end{bmatrix} \begin{bmatrix} \mathbf{v}^{n+1} \\ \mathbf{p}^{n+1} \end{bmatrix} = \begin{bmatrix} \mathbf{r}^n \\ \mathbf{0} \end{bmatrix} + \begin{bmatrix} \mathbf{bc}_1 \\ \mathbf{bc}_2 \end{bmatrix} \tag{4.18}$$

$$\text{with } \mathbf{r}^n = \Delta t \left[\mathbf{M}_\rho \mathbf{v}_d^n + \frac{1}{Fr^2} \mathbf{M}_\rho \mathbf{g}^n + \frac{1}{We} \mathbf{M} \mathbf{f}^n \right],$$

where $\mathbf{bc}_1, \mathbf{bc}_2$ are vectors accounting for Dirichlet boundary conditions of velocity and pressure respectively, if any. Recalling that the interfacial force is given by Equation (3.38), in order to obtain its discrete version to accompany the We number, the following matrix equation is written

$$\mathbf{M} \mathbf{f}^n = \mathbf{\Sigma} \mathbf{G} \mathbf{h}^n, \tag{4.19}$$

where $\mathbf{\Sigma} = \sigma \kappa(\mathbf{x}_j) \mathbf{I}$ is a diagonal matrix storing the surface tension and curvature effects distributed for all the mesh nodes and $\mathbf{h}^n$ the discrete vector of the Heaviside function. Consequently, the vector $\mathbf{r}^n$ in Equation (4.18) takes the form

$$\mathbf{r}^n = \Delta t \left[\mathbf{M}_\rho \mathbf{v}_d^n + \frac{1}{Fr^2} \mathbf{M}_\rho \mathbf{g}^n + \frac{1}{We} \mathbf{M}_L^{-1} \mathbf{\Sigma} \mathbf{G} \mathbf{h}^n \right],$$

now containing the inverse lumped matrix $\mathbf{M}_L^{-1}$.

Taking advantage of the discussion in Subsection 3.2.1, the governing equations are now viewed under a projection-like fully discretized format appropriate to the resulting process derived from the FE intervention,

$$\mathbf{M}_{NS} \mathbf{v}_{NS} = \mathbf{b}_{NS}, \tag{4.20}$$

with

$$\mathbf{M}_{NS} = \begin{bmatrix} \mathbf{B} & -\Delta t \mathbf{G} \\ \mathbf{D} & \mathbf{0} \end{bmatrix}; \qquad \mathbf{v}_{NS} = \begin{bmatrix} \mathbf{v}^{n+1} \\ \mathbf{p}^{n+1} \end{bmatrix}; \qquad \mathbf{b}_{NS} = \begin{bmatrix} \mathbf{r}^n \\ \mathbf{0} \end{bmatrix} + \begin{bmatrix} \mathbf{bc}_1 \\ \mathbf{bc}_2 \end{bmatrix}, \tag{4.21}$$

whence comes out the following exact LU factorization of $\mathbf{M}_{NS}$ based on lumping process of the mass matrix $\mathbf{M}_\rho$ (cf. [?]):

$$\begin{bmatrix} \mathbf{B} & \mathbf{0} \\ \mathbf{D} & \Delta t \mathbf{DM}_{\rho,L}^{-1}\mathbf{G} \end{bmatrix} \begin{bmatrix} \mathbf{I} & -\Delta t \mathbf{M}_{\rho,L}^{-1}\mathbf{G} \\ \mathbf{0} & \mathbf{I} \end{bmatrix} \begin{bmatrix} \mathbf{v}^{n+1} \\ \mathbf{p}^{n+1} \end{bmatrix} = \begin{bmatrix} \mathbf{r}^n \\ \mathbf{0} \end{bmatrix} + \begin{bmatrix} \mathbf{bc}_1 \\ \mathbf{bc}_2 \end{bmatrix}, \tag{4.22}$$

The lumping technique minimizes the computational cost of inverting $\mathbf{M}_\rho$.

Following the straightforward LU scheme, the solution of Equation (4.22) is bipartite. Firstly, the system

$$\begin{bmatrix} \mathbf{B} & \mathbf{0} \\ \mathbf{D} & \Delta t \mathbf{DM}_{\rho,L}^{-1}\mathbf{G} \end{bmatrix} \begin{bmatrix} \mathbf{v}^{\#} \\ \mathbf{p}^{n+1} \end{bmatrix} = \begin{bmatrix} \tilde{\mathbf{b}}_1 \\ \mathbf{bc}_2 \end{bmatrix}; \qquad \tilde{\mathbf{b}}_1 = \mathbf{r}^n + \mathbf{bc}_1 \tag{4.23}$$

for the intermediary velocity $\mathbf{v}^{\#}$ and the pressure $\mathbf{p}^{n+1}$ is solved. Chang *et al.* [?] reports that the error due to the splitting process affecting this classic fractional step method is reduced if a unique matrix – in this case, $\mathbf{M}_{\rho,L}^{-1}$ –, is interspersed in the LU scheme. The shortcoming for the velocity field is corrected posteriorly. Secondly, the system

$$\begin{bmatrix} \mathbf{I} & -\Delta t \mathbf{M}_{\rho,L}^{-1}\mathbf{G} \\ \mathbf{0} & \mathbf{I} \end{bmatrix} \begin{bmatrix} \mathbf{v}^{n+1} \\ \mathbf{p}^{n+1} \end{bmatrix} = \begin{bmatrix} \mathbf{v}^{\#} \\ \mathbf{p}^{n+1} \end{bmatrix} \tag{4.24}$$

is solved to find the actual values of the fields.

From Equations (4.23) and (4.24), the following routine of calculations can be posed:

$$\text{Solve} \quad \mathbf{B}\mathbf{v}^{\#} = \tilde{\mathbf{b}}_1; \tag{4.25}$$

$$\text{Solve} \quad \tilde{\mathbf{E}}\mathbf{p}^{n+1} = \tilde{\mathbf{b}}_2; \quad \text{with} \quad \tilde{\mathbf{E}} = \Delta t \mathbf{DM}_\rho^{-1}\mathbf{G}; \quad \tilde{\mathbf{b}}_2 = \tilde{\mathbf{bc}}_2 - \mathbf{D}\mathbf{v}^{\#}; \tag{4.26}$$

$$\text{Correct} \quad \mathbf{v}^{n+1} = \mathbf{v}^{\#} + \Delta t \mathbf{M}_\rho^{-1}\mathbf{G}\mathbf{p}^{n+1}. \tag{4.27}$$

However, Anjos [?] generalizes the correction of the intermediary velocity field when gravity forces and interfacial forces are assumed in the modelling of two-phase flows. The incremental

term e, which comes into the correction equation determines a substep for the projection method resulting in

$$\mathbf{v}^{\#}_{corr} = \mathbf{v}^{\#} + \Delta t e(\mathbf{g}, \mathbf{f}, Fr, We) \qquad (4.28)$$

and its form depends on the forces $\mathbf{g}$, $\mathbf{f}$, the Fr and We numbers as well as on the nature of the flow. For pure single-phase flows without the introduction of the pressure gradient term (discussed in the next chapter), $\mathbf{v}^{\#}_{corr}$ reduces to $\mathbf{v}^{\#}$.

4.3.2 <u>Fluid variables</u>

To obtain a variational form for the advection-diffusion equation liable to model the transport of variables immersed in a carrying fluid, we proceed similarly to the previous essay. Then, we begin by introducing the Sobolev space

$$\mathscr{R} := \left\{ r \in \mathscr{L}^2(\Omega) \, ; \, r = 0 \, \text{in} \, \Gamma_D \right\}$$

of weight functions. Therefrom, the finite space $\mathscr{R}^h \subset \mathscr{R}$. In turn, we weight the Equation (3.31) to have

$$\int_\Omega \frac{D\Psi}{Dt} r \, dV = \frac{1}{ReSc} \int_\Omega \nabla^2 \Psi \, r \, dV, \quad r \in \mathscr{R}. \qquad (4.29)$$

Then, by analogous reasoning, the bilinear forms coming after using Equation (4.13) for $u = \Psi$ in the weighted global formulation Equation (4.29) via Galerkin produce the discrete equation

$$m_\Psi \left(\frac{\hat{D}\Psi_h}{Dt}, r_h \right) + \frac{1}{ReSc} k_\Psi(\varrho; \nabla \Psi_h, \nabla r_h) = 0, \qquad (4.30)$$

whereof

$$m_\Psi \left(\Psi_h^{n+1}, r_h \right) + \frac{\Delta t}{ReSc} k_\Psi(\varrho; \nabla \Psi_h^{n+1}, \nabla r_h) = \Delta t \, m_\Psi(\Psi_{h,d}^n, r_{h,P}). \qquad (4.31)$$

By writing the matrix form, we have

$$\mathbf{M}_\Psi \mathbf{\Psi}^{n+1} + \frac{\Delta t}{ReSc} \mathbf{K}_\Psi \mathbf{\Psi}^{n+1} = \Delta t \mathbf{M}_\Psi \mathbf{\Psi}_d^n, \qquad (4.32)$$

or, with $\mathbf{B}_\Psi = \mathbf{M}_\Psi + \frac{\Delta t}{ReSc}\mathbf{K}_\Psi$, the form

$$\mathbf{B}_\Psi \mathbf{\Psi}^{n+1} = \mathbf{r}_\Psi^n + \mathbf{bc}_\Psi, \tag{4.33}$$

for

$$\mathbf{r}_\Psi^n = \Delta t \mathbf{M}_\Psi \mathbf{\Psi}_d^n \tag{4.34}$$

and $\mathbf{bc}_\Psi$ a vector containing Dirichlet boundary conditions. Along with Equation (4.18), Equation (4.33), form a system of FE-based ordinary equations as

$$\begin{cases} \mathbf{Bv}^{n+1} + \Delta t \mathbf{Gp}^{n+1} = \mathbf{r}^n + \mathbf{bc}_1 \\ \qquad\qquad \mathbf{Dv}^{n+1} = \mathbf{0} + \mathbf{bc}_2 \\ \qquad\quad \mathbf{B}_\Psi \mathbf{\Psi}^{n+1} = \mathbf{r}_\Psi^n + \mathbf{bc}_\Psi \end{cases} \tag{4.35}$$

with a group of generalized discrete initial and boundary conditions

$$\begin{cases} \mathbf{v}_{i,0} = \mathbf{v}_0, \\ \mathbf{p}_{j,0} = \mathbf{p}_0, \\ \mathbf{\Psi}_{j,0} = \mathbf{\Psi}_0 \\ \\ \mathbf{v}_i|_{\Gamma_{D\vee N}^2} = \mathbf{v}_{D\vee N}^{\Gamma^2} \\ \mathbf{p}_j|_{\Gamma_{D\vee N}^2} = \mathbf{p}_{D\vee N}^{\Gamma^2} \\ \mathbf{\Psi}_j|_{\Gamma_{D\vee N}^2} = \mathbf{\Psi}_{D\vee N}^{\Gamma^2} \end{cases} \tag{4.36}$$

for $i = 1, 2, \dots, \iota_v$; $j = 1, 2, \dots, \iota_s$ whose discrete solution for each unknown DOF over the mesh is the triple $(\mathbf{v}, \mathbf{p}, \mathbf{\Psi})$. Here, two remarks are enriching: i) Dirichlet or Neumann boundaries can be chosen provided that they are consistently imposed; ii) $\dim(\mathbf{v}) = 3\iota_v$, whereas $\dim(\mathbf{p}) = \dim(\mathbf{\Psi}) = \iota_s$.

4.3.3 The stable MINI element 3D

The Navier-Stokes equations belong to a mixed universe, so that a FE space that deals with the coupling velocity/pressure is required. Moreover, stability criteria need to be satisfied for such space. To attire and complete the theoretical development of Section 4.3,

we call up some information about the Taylor-Hood's family MINI element, which drives the element-level discretization of the presented formulation.

In $\mathbb{R}^3$, the MINI element is a tetrahedron containing DOFs at its vertices and at the barycenter (see Figure 26) whose shape functions are similar to "bubbles". According to the Taylor-Hood approach (cf. [?], p. 174), the velocity field is approximated by a first order polynomial set enriched with functions formed by combining the barycentric coordinates, while the pressure field has only a first-order accuracy. Furthermore, it was proved that the
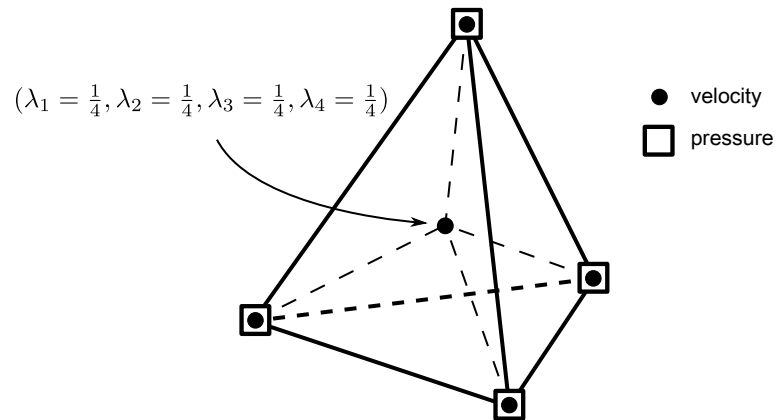

Figure 26: MINI element 3D highlighting the sites for the degrees of freedom of velocity and pressure.

MINI element fulfills the requirements of stability also known as the *LBB* condition [?], [?], [?]. Mathematically, if defined, for $k \geq 1$ the set

$$\mathcal{M}_0^k(\mathcal{T}^h) = \{\mathbf{v}; \mathbf{v} \in C^0(\Omega), \ \mathbf{v}|_T \in P_k(T) \ \forall T \in \mathcal{T}_h\}$$
$$\mathring{\mathcal{M}}_0^k(\mathcal{T}^h) = \mathcal{M}_0^k(\mathcal{T}^h) \cap \mathcal{H}_0^1(\Omega),$$

and for $k \geq 3$ the set

$$\mathcal{B}^k(\mathcal{T}^h) = \{\mathbf{v}|\mathbf{v}|_T \in \mathscr{P}_k(T) \cap \mathcal{H}_0^1(T) \ \forall T \in \mathcal{T}^h\},$$

when $k = 3$, a bubble function proportional to the barycentric coordinates as $\lambda_1\lambda_2\lambda_3\lambda_4$ lies over the barycenter ($\lambda_j = \frac{1}{4}, 1 \leq j \leq 4$) of the tetrahedron. Then, the MINI element ($m = 3$) uses the FE spaces

$$\mathcal{V}^h = \{(\mathring{\mathcal{M}}_0^1) \times (\mathring{\mathcal{M}}_0^1) \times (\mathring{\mathcal{M}}_0^1)\} \oplus \{\mathcal{B}^3 \times \mathcal{B}^3 \times \mathcal{B}^3\}$$
$$\mathcal{Q}^h = \mathcal{M}_0^1$$

and evaluates 13 DOFs per element to solve a full system like Equation (4.36). In this case, the DOFs corresponding to the scalar field are evaluated at the vertices of the tetrahedron, just as the DOFs of pressure, forcing the storage of $3\iota_v + 2 \times 4\iota_s = 3\iota_v + 8\iota_s$ equations in the computer's memory.

4.4 Dynamic mesh control and ALE parametrization

Many geometrical operations are performed behind the ALE code used in this thesis, mainly due to the dynamic movement of the computational FE mesh. This heavy load of numerical work, namely: displacement, insertion, deletion and rearrangement of nodes; contraction and flipping of edges; smoothing and redistribution of velocity fields, or even mesh quality checking routines require, above all, a physical background upon the flow under examination.

A expression describing the arbitrary movement of a mesh can be given by

$$\hat{\mathbf{v}} = \alpha_1 \mathbf{v} + \alpha_2 \mathbf{v}_e, \quad 0 \le \alpha_1, \alpha_2 \le 1, \tag{4.37}$$

for which the real parameters α_1, α_2 balance the mesh velocity to determine intermediary motions that differ from a completely Lagrangian or Eulerian one. Thus, if $\alpha_1 = 0$ and $\alpha_2 = 1$, for instance, a purely elastic motion is achieved, whose interpretation depends on the techniques applied for the mesh treatment. Notwithstanding the free choice of these parameters, higher flexibility is attained when their values are different from zero.

Following the generalized ALE method presented by [?], it is assumed here that the mesh velocity is made up by partial velocities, each of them ascribed according to the flow physics. Given that the computational mesh was defined by Equation (2.23) as the union of two subsets, different mesh operations are allocated for them independently. Thus, the mesh velocity is governed by the following general form:

$$\hat{\mathbf{v}}(\mathbf{x}_j) = \begin{cases} \mathbf{v} - \gamma_1(\mathbf{v} \cdot \mathbf{t})\mathbf{t} + \gamma_2(\mathbf{v}_e \cdot \mathbf{t})\mathbf{t} & , \text{ if } \mathbf{x}_j \in \mathscr{T}_{h_1}^{\Gamma^1} \\ \beta_1 \mathbf{v} + \beta_2 \mathbf{v}_{I;\epsilon} + \beta_3 \mathbf{v}_e & , \text{ otherwise} \end{cases} \tag{4.38}$$

with $\mathbf{t}$ being a unit vector on the tangent plane to the interface at $\mathbf{x}_j = \mathbf{x}_I$. Apart from any simplicity, this generalized method holds intricate calculations to guarantee an interface

representation highly accurate through nodal scattering. As seen, Equation (4.38) works differently for the mesh subsets. Therefore, a brief description of how each parcel interferes on the scheme is serviceable (cf. [?], ch. 6).

By analyzing the first condition, for interface nodes, we note that $\hat{\mathbf{v}}$ is made up by the fluid velocity, the tangential component of the fluid velocity and the tangential component of the elastic velocity. More precisely, once the decomposition

$$\mathbf{v}_I = (\mathbf{v} \cdot \mathbf{t})\mathbf{t} + (\mathbf{v} \cdot \mathbf{n})\mathbf{n} \Rightarrow \tag{4.39}$$

$$\mathbf{v}_{I,\mathbf{n}} = \mathbf{v}_I - (\mathbf{v} \cdot \mathbf{t})\mathbf{t}, \tag{4.40}$$

is valid for any interface node, it turns out that the parameter γ_1 is associated to the reduction of the tangent interface nodal velocity on the flow so that the two first terms of this condition are combined into one effect, *viz.* of allowing that the interface moves in the normal direction with higher relaxation. Oppositely, γ_2 is the parameter responsible for the intensity of mesh smoothing driven by the elastic velocity $\mathbf{v}_e$.

On the other hand, the second condition, for volumetric nodes, aggregates components depending on the fluid velocity, the elastic velocity and the additional smoothing velocity $\mathbf{v}_{I;\epsilon}$ resulting from the contribution of the interface neighbourhood ϵ, which we will name "neighbourhood-based velocity". In turn, it turns out that β_1 controls the Lagrangian motion of the volume mesh, whereas β_2, β_3 manage the intensity of mesh smoothing driven by the neighbourhood-based velocity $\mathbf{v}_{I;\epsilon}$, and the elastic velocity, respectively.

4.4.1 Dynamic control techniques

In this thesis, a scheme of Laplacian smoothing is used to relocate the mesh nodes and achieve qualitative elements through volume restriction and aspect ratio control. By considering $\mathsf{S}(i)$ the "star" of the node i (elements sharing i as a common vertex), the technique for relocation of points is given by

$$\mathbf{x}_i \to \hat{\mathbf{x}}_i := \sum_{j \in \mathsf{S}(i)}^{\#\mathsf{S}} w_{ij}(\mathbf{x}_j - \mathbf{x}_i), \quad w_{ij} = l_{ij}^{-1}, \tag{4.41}$$

meaning that $\mathbf{x}_i$ moves to the new position $\hat{\mathbf{x}}_i$ within each remeshing operation. Additionally, l_{ij} is the length of the edge joining the central node i to each node j encircling it at the star as
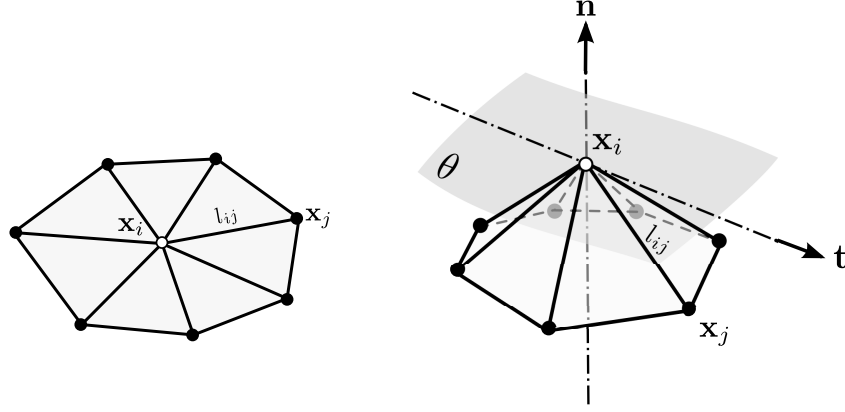
displayed in Figure 27.

Figure 27: Representations of the star $\mathsf{S}(i)$ of the node i: 2D version at left and 3D version with the tangent plane θ at right.

Both the elastic velocity $\mathbf{v}_e$ and the neighbourhood-based velocity $\mathbf{v}_{I;\epsilon}$ play a remarkable role as mesh smoothing appliances. While the former is obtained from an approximation via uniform motion within each discrete time Δt, the latter is computed through the arithmetic mean among the neighbour's velocities which are immersed into the continuous phase, thus taking the near-field dynamics into account for the interface motion. Sequentially, they are defined, for each node i as

$$\mathbf{v}_e(i) = \frac{1}{\Delta t} \sum_{j \in \mathsf{S}(i)}^{\#\mathsf{S}} l_{ij}^{-1}(\mathbf{x}_j - \mathbf{x}_i) \tag{4.42}$$

$$\mathbf{v}_{I;\epsilon}(i) = \frac{1}{\#\mathsf{S}} \sum_{j \in \mathsf{S}(i)}^{\#\mathsf{S}} \mathbf{v}_j \tag{4.43}$$

4.4.2 Geometrical operations and remeshing appliances

To gauge harsh topological changes that an interface may undergo in virtue of the hydrodynamics, geometrical operations are performed over the elements of the discrete interface. Among the various appliances of the ALE/FE method discussed here, which are intended to preserve the mesh quality as best as possible, the main operations deserving particular attention are: node insertion (Υ^+), node deletion (Υ^-), edge contraction ($\Xi^{\asymp}$) and edge flipping ($\Xi^{\emptyset}$) as depicted in Figure 28. For each case, a minimal patch of elements is used as model. Such operations, symbolized by Υ^+, Υ^-, $\Xi^{\asymp}$ and $\Xi^{\emptyset}$ can be interpreted as functions whose arguments are nodes and/or edges of the interface discrete mesh. In 3D simulations, many topological complications may arise at element-level due to inaccuracies
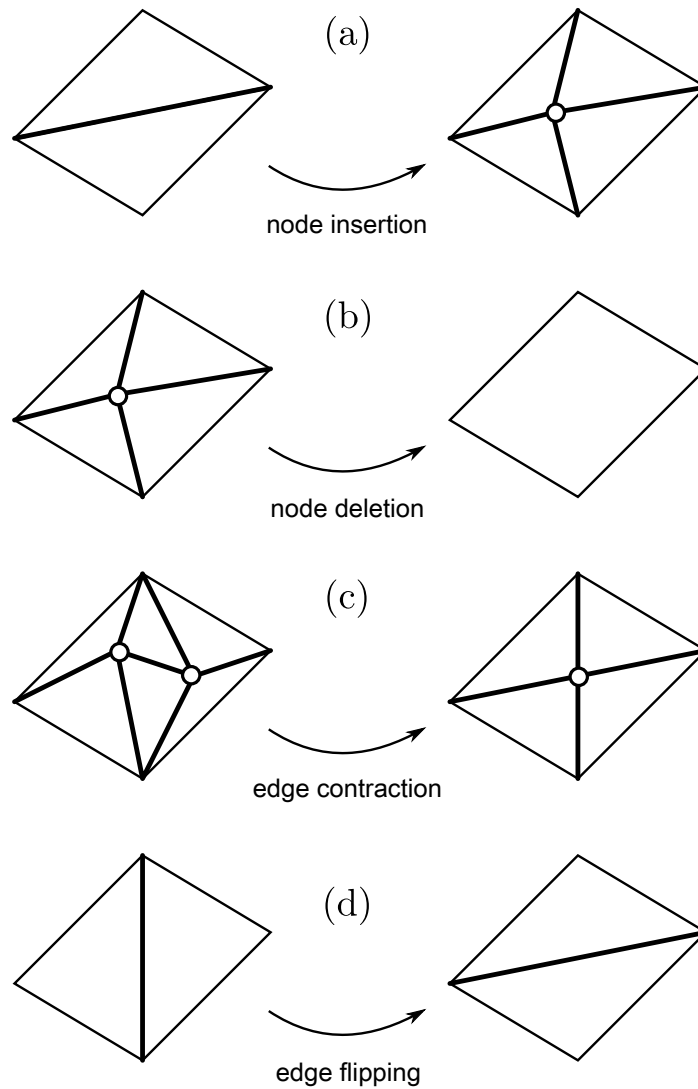
Figure 28: Possible range of geometrical operations for the discrete interface: (a) node insertion; (b) node deletion; (c) edge contraction; (d) edge flipping.

in capturing high curvatures zones or degenerate elements. Due to that wide range of possible configurations for the elements, challenging and exhaustive black-box tests are required to remedy all the potential remeshing failures. In summary, Table 1 gathers the main code objects related to the dynamic mesh control.

4.5 **Solvers and preconditioning**

Not only due to the ALE remeshing operations, but also the refinement levels imposed over the mesh, the global linear systems generated through FE may render huge, i.e. to contain many DOFs. Avoiding time-consuming solutions and sparsity problems is a task which needs of optimal combinations between solver/preconditioner. In this thesis, solvers

Symbol	Description
β_1	pure Lagrangian motion control
β_2	neighbourhood-based velocity smoothing
β_3	elastic-based velocity Laplacian smoothing
γ_1	tangent interface velocity magnitude control
γ_2	elastic-based velocity and mesh quality
Υ^+	node insertion operator
Υ^-	node deletion operator
$\Xi^{\asymp}$	edge contraction operator
$\Xi^{\lozenge}$	edge flipping operator

Table 1: ALE meshing parameters for surface operations.

and preconditioners based on Krylov spaces from the PETSC library [?] were used. Although a comparative study was not performed to find the better combination, better results were achieved by using Pre-Conjugated Gradient (PCG) solvers together with Incomplete Cholesky (ICC) or Incomplete LU (ILU) preconditioners.